

## **General Disclaimer**

### **One or more of the Following Statements may affect this Document**

- This document has been reproduced from the best copy furnished by the organizational source. It is being released in the interest of making available as much information as possible.
- This document may contain data, which exceeds the sheet parameters. It was furnished in this condition by the organizational source and is the best copy available.
- This document may contain tone-on-tone or color graphs, charts and/or pictures, which have been reproduced in black and white.
- This document is paginated as submitted by the original source.
- Portions of this document are not fully legible due to the historical nature of some of the material. However, it is the best reproduction available from the original submission.

TO: NASA Langley Research Center  
Hampton, Virginia 23665

(NASA-CR-157767) EARLY STAGES OF THE  
OXIDATION OF METAL SURFACES Final Report,  
Oct. 1976 - 30 Sep. 1978 (Massachusetts  
Inst. of Tech.) 100 p HC A05/MF A01

N78-33195

Unclas  
CSCL 11F G3/26 33819

EARLY STAGES OF THE OXIDATION OF METAL SURFACES

Grant No. NSG 1337

Final Report

Period October 1, 1976 to September 30, 1978



Submitted by

Professors H. C. Gatos and K. H. Johnson  
Department of Materials Science and Engineering  
Massachusetts Institute of Technology  
Cambridge, Massachusetts 02139

## EARLY STAGES OF THE OXIDATION OF METAL SURFACES

Photoemission cross sections have been calculated for the  $\text{ZnO}_4^{-6}$  cluster using the Self-Consistent- $\chi\alpha$ -Scattered Wave (SCF- $\chi\alpha$ -SW) theory which display the main features of the ultraviolet and X-ray photoemission data from ZnO. A solid model is suggested for an absolute photoemission intensity comparison resulting in  $\lambda\alpha$  intensities which are roughly 70% of the experimental values. Together with the experimental data, the calculations allow a complete determination of the electronic structure of a ZnO surface.

TABLE OF CONTENTS

	Page
TITLE PAGE. . . . .	1
ABSTRACT. . . . .	2
TABLE OF CONTENTS . . . . .	3
LIST OF TABLES AND FIGURES. . . . .	5
CHAPTER ONE. INTRODUCTION. . . . .	7
CHAPTER ONE REFERENCES. . . . .	13
CHAPTER TWO. PHOTOEMISSION . . . . .	14
CHAPTER TWO REFERENCES. . . . .	21
CHAPTER THREE. SCF- $\gamma$ $\alpha$ -SW METHOD. . . . .	24
3.1. Solutions for Region I. . . . .	26
3.2. Solutions for Region III . . . . .	27
3.3. Solutions for Region II . . . . .	28
3.4. Total Solutions. . . . .	30
3.5. Matrix Elements. . . . .	32
CHAPTER THREE REFERENCES. . . . .	35
CHAPTER FOUR. PREVIOUS ZnO STUDIES . . . . .	36
4.1. Photoemission. . . . .	36
4.1.1. Experimental Uncertainties. . . . .	37
4.1.2. Spectrometer Transmission and Broadening. . . . .	38
4.1.3. Work Function and Threshold. . . . .	40
4.1.4. Ultra High Vacuum Requirements. . . . .	41

	Page
4.2. ZnO Photoemission Experimental Studies. . . . .	42
4.3. Optical Experimental Studies. . . . .	44
4.4. Theoretical Studies. . . . .	44
CHAPTER FOUR REFERENCES. . . . .	51
CHAPTER FIVE. PRESENT STUDY. . . . .	52
5.1. Choice of Parameters. . . . .	52
5.2. Orbital Structure of ZnO. . . . .	54
5.2.1. Comparison of Theoretical and Experimental Orbital Structure. . . . .	56
5.3. Generation of X $\alpha$ Photoemission Spectra. . . . .	61
5.4. UV Photoemission Cross Sections. . . . .	62
5.4.1. Upper Valence Band . . . . .	62
5.4.2. Zn 3d Band. . . . .	73
5.5. Xray Photoemission Cross Sections . . . . .	76
5.5.1. Modulating Effects. . . . .	82
5.6. UV Intensity Comparison . . . . .	83
5.6.1. Solid Model from Clusters . . . . .	86
5.6.2. Solid Model Cross Sections. . . . .	90
5.7. Conclusion. . . . .	93
5.8. Summary. . . . .	96
CHAPTER FIVE REFERENCES. . . . .	97
APPENDIX A. . . . .	98
APPENDIX B. . . . .	99
ACKNOWLEDGEMENTS. . . . .	100 . . . . .

LIST OF TABLES AND FIGURES

- Figure 4.2(a) Energy-loss spectrum of ZnO.  
                  (b) Reflectivity spectrum of ZnO.
- Figure 4.3(a) Energy band diagram of ZnO, KKR method.  
                  4.3(b) Energy band diagram of ZnO, Pseudo-potential method.
- Figure 4.4 Molecular orbital diagram of ZnO, SCF- $\chi\alpha$ -SW method.
- Figure 5.1 Surface structure of wurtzite ZnO.
- Table 5.1 Comparison of theoretical and experimental electron energy levels.
- Figure 5.2 Molecular orbital diagram of  $\text{ZnO}_4^{-6}$ .
- Figure 5.3  $\chi\alpha$  generated ultraviolet energy distribution curves for  $\text{ZnO}_4^{-6}$ .
- Figure 5.4 Ultraviolet experimental energy distribution curves for ZnO.
- Figure 5.5(a) Photoemission cross sections for the  $7t_2$  orbital.
- Figure 5.5(b) Photoemission cross sections for the  $1t_1$  orbital.
- Figure 5.5(c) Photoemission cross sections for the  $2e$  orbital.
- Figure 5.5(d) Photoemission cross sections for the  $6t_2$  orbital.
- Figure 5.5(e) Photoemission cross sections for the  $6a_1$  orbital.
- Figure 5.5(f) Photoemission cross sections for the  $1e$  orbital.

- Figure 5.5(g) Photoemission cross sections for the  $5t_2$  orbital.
- Figure 5.6  $\chi\alpha$  generated X-ray spectra for  $\text{ZnO}_4^{-6}$ .
- Figure 5.7 Experimental X-ray spectra for ZnO.
- Figure 5.8 Curvature comparison of initial and final states.
- Figure 5.9 Electron scattering lengths.
- Figure 5.10 Solid model diagram.
- Figure 5.11 Solid model spectra.
- Figure 5.12 Solid model and experimental spectra comparison.
- Figure 5.13 Electronic structure of ZnO.

## CHAPTER ONE

### INTRODUCTION

Surface studies have increased dramatically in the past few years, especially in the areas of adsorption and chemisorption on metallic surfaces. An understanding of the geometric and electronic structure of surfaces is of paramount importance in the study of catalytic processes, corrosion, passivity, and oxidation.

In solid state physics, the bulk characteristics of metals have been successfully studied by assuming a geometry from X-ray scattering and then calculating a cohesive energy. Gases have been studied by rotational spectroscopy (infrared) to obtain their geometrical arrangement. However, the study of gases adsorbed on metal surfaces is much more complicated because the molecules do not rotate freely on surfaces, and the metal electrons screen the electric field of the incident light.<sup>1</sup>

Low energy electron diffraction (LEED)<sup>2</sup> has provided the most extensive geometric information concerning surfaces. In LEED, electrons with wavelengths comparable to the lattice spacing are scattered by the ion cores of the periodic crystal. This corresponds to an energy range of 10 eV to 500 eV, where the electrons have a mean free path



of 3-20 Å. Thus virtually all the scattering is within the surface region. However, difficulty arises due to multiple scatterings.

Photoelectron spectroscopy<sup>3</sup> (photoemission) has proven to be the most promising technique for the determination of the energy levels. The incident light is in the ultraviolet or soft X-ray region, and the current of photoemitted electrons is measured as a function of their kinetic energy. Then the binding energy is given by

$$E_b = \hbar\omega - E_k \quad (1.1)$$

where  $\hbar\omega$  is the energy of the incident light and  $E_k$  is the kinetic energy of the photoemitted electron. This method is surface sensitive even though the light penetrates into the solid because the photoemitted electrons have a short mean free path. It is important to remember that the peaks in the measured spectrum correspond to the various states of the ion whereas the neutral system is of direct interest. However, in most cases the states of the ion can be correlated with those of the neutral system so that the spectrum gives a picture of the energy levels of the neutral system.

Most of the experimental work in photoelectron spectroscopy has involved measuring the binding energies using either He I(21.2 eV) or He II(40.8 eV) resonance lamps.

However, with the use of synchrotron radiation the continuous range from the infrared to the X-ray region is now available.

A further advance has been to measure the photoelectron spectrum as a function of take off angle for the emitted electron and as a function of the angle of incidence for the incoming light. With the use of highly polarized and tunable light, measurements can be made as a function of photon energy with angular dependences as well. If a gaseous molecule adsorbed on a solid surface has a definite orientation, distinctive angular patterns can be observed which would not be present for the random orientations of the gas phase. These patterns are not simply related to any physical property of the system but are given by the matrix element of the photoemission Hamiltonian between initial and final (continuum) states. Thus it is essential to have a theory of photoemission in order to extract useful physical information.

Our photoemission calculations were performed using the Self-Consistent-Field- $\chi\alpha$ -Scattered Wave (SCF- $\chi\alpha$ -SW) method. This method yields quite good ionization potentials and charge densities yet is sufficiently economical to be applied to relatively large systems. The multiple scattering method has been developed over the years, both in

nuclear physics<sup>4</sup> to compute nuclear cross sections, and in solid state physics<sup>5</sup> to compute the electronic structure of solids. More recently the method has been applied to molecular physics by Johnson and coworkers<sup>6,7</sup> to calculate bound state eigenvalues. These eigenfunctions serve as the initial state in the matrix element of photoemission. The final states are calculated by the extension of the multiple scattering method developed by Dill and Dehmer<sup>8</sup> to treat unbound states. Finally, the multiple scattering theory has been applied to surface physics by Davenport<sup>9</sup> to calculate matrix elements of photoemission cross sections.

For the case of semiconductors, photoemission is generally considered to be a "local" process. Thus it is quite reasonable to expect the cluster approach to provide a better description than that of band theory, which depends on long range order and periodicity. Indeed, photoemission cross section calculations have been performed on the CO molecule using the SCF- $\chi\alpha$ -SW cluster model which for the first time place theory and experiment in reasonable agreement.<sup>11</sup> These calculations were able to determine the orientation of undissociated CO molecules on a solid surface.<sup>10</sup> In this case the substrate can be neglected in the calculation because the energy levels of

the adsorbate are relatively unperturbed upon adsorption. Thus these calculations can provide only geometrical arrangement of the surface but do not provide any information on the electronic structure of the "adsorptive" bonds.

The next step is to calculate cross sections for the more complicated case of adsorption whereupon the adsorbing molecule does dissociate and thus the substrate cannot be neglected. This is the more general case of chemisorption and can provide information on both the geometric and electronic structure.

In this dissertation we discuss our SCF- $\chi\alpha$ -SW photoemission cross section calculations for the case of adsorption of a dissociated molecular species on a metallic surface. We have chosen to use a zinc surface since it is representative of a nontransition metal and also because of its technological importance concerning catalytic processes. We have chosen to use oxygen as the adsorbing gas because of its importance involving corrosion. The ZnO system is a good choice since both ultraviolet (UV) and X-ray experimental photoemission data is available for comparison. Differential cross sections were not calculated for ZnO since no experimental data has been published.

The structure of the remainder of this dissertation is as follows. In Chapter 2 we discuss the theory of photo-

emission and briefly review previous calculations in the literature. In Chapter 3 we develop the formalism for the SCF- $\chi\alpha$ -SW method of photoemission. Chapter 4 is a brief summary of photoemission experimental methods and of relevant surface studies done previously on the ZnO system. In Chapter 5 we present our results and conclusions.

ORIGINAL PAGE IS  
OF POOR QUALITY

CHAPTER ONE REFERENCES

1. J.T. Yates, Jr., R.G. Greenler, I. Ratajczyk and D.A. King, Surf. Sci. 36, 739 (1973).
2. M.B. Webb and M.G. Lagally, Solid State Physics 28, 301 (1973).
3. E.W. Plummer in Topics in Applied Physics 4, 143 (1975) (Springer-Verlag, N.Y., 1975).
4. D. Agassi and A. Gal, Ann. Phys. (N.Y.) 75, 561 (1973) and references 1 and 2 therein.
5. P.M. Mores, Proc. Natl. Acad. Sci. U.S. 42, 276 (1956); W. Kohn and N. Rostoker, Phys. Rev. 94, 1111 (1954); J. Korringa, Physica 13, 392 (1947).
6. K.H. Johnson, J. Chem. Phys. 45, 3085 (1966).
7. K.H. Johnson and F.C. Smith, Jr., Chem. Phys. Letters 7, 541 (1970).
8. D. Dill and J.L. Dehmer, J. Chem. Phys. 61, 692 (1974).
9. J.W. Davenport, Dissertation, Univ. of Pa., Philadelphia, Pa. 1976.
10. J.W. Davenport, Phys. Rev. Lett. 36, 945 (1976).
11. G. Apai, P.S. Wehner, R.S. Williams, J. Stohr and D.A. Shirley, Phys. Rev. Lett. 37, 1497 (1976).

## CHAPTER TWO

PHOTOEMISSION

The differential photoemission cross section is defined as the number of electrons leaving the sample which flow into a given solid angle per unit time divided by the number of photons incident on the sample per unit area and per unit time:

$$\frac{d\sigma}{d\Lambda} = \frac{N_{\text{electrons}}}{N_{\text{photons/Area}}}$$

The total cross section (also called angle averaged cross section) is obtained by integrating over all solid angles and is usually in the range of 1-20 megabarns, where  $1 \text{ Mb} = 10^{-18} \text{ cm}^2$ .

The Hamiltonian for photoemission can be written

$$H = H_0 + \frac{e}{mc} \vec{A} \cdot \vec{p} - i \frac{eh}{2mc} \vec{\nabla} \cdot \vec{A} + \frac{e^2}{2mc^2} |\vec{A}|^2 \quad (2.1)$$

which is just the one electron Hamiltonian for a molecule in the presence of the field  $\vec{p} \rightarrow \vec{p} + \frac{e}{c} \vec{A}$ . We will consider a nonquantized radiation field which is valid for arbitrary light intensities involving induced emission processes.<sup>1</sup> The last term in Eq. 2.1 is the diamagnetic term which is small and will be neglected. We will make the dipole approximation, i.e., neglect the spatial variation of the

vector potential  $\vec{A}$  within the matrix element, which is reasonable when the incident radiation wavelengths are large compared to the atomic dimensions. Then the term in  $\vec{\nabla} \cdot \vec{A}$  will be zero, and the Hamiltonian consists of

$$H = H_0 + \frac{e}{mc} \vec{A} \cdot \vec{p}$$

where  $H_0 = \frac{\vec{p}^2}{2m} + V(\vec{r})$  and  $\frac{e}{mc} \vec{A} \cdot \vec{p}$  can be considered as a perturbation term.  $\hat{A}$  is the unit vector in the direction of  $\vec{A}$ .

The transition probability between eigenfunctions  $|i\rangle$  and  $|f\rangle$  of  $H_0$  is obtained from Fermi's Golden rule<sup>2</sup>

$$\frac{dw}{dt} \sim \sqrt{\epsilon_k} \sum_k \delta(\epsilon_f - \epsilon_i - \hbar\omega) |\langle f | \vec{\nabla} \cdot \vec{A} | i \rangle|^2$$

The matrix element is correct only to first order since  $|i\rangle$  and  $|f\rangle$  are eigenfunctions of  $H_0$  and not of the perturbation term. In actual calculations however,  $|i\rangle$  is a numerical solution to an approximated  $H_0$  and represents a bound state whereas  $|f\rangle$  is a function of the wave vector  $\vec{k}$  of the photoemitted electron and represents a continuum state. The search for an appropriate form of the final state  $|f\rangle$  has been the aim of past photoemission calculations. Bethe and Salpeter<sup>3</sup> have calculated cross sections of hydrogenic levels using plane wave final states. They show that



the plane wave results never approach the correct value, except for s states and then only in the high frequency limit  $\sim 500$  eV. The final state we will use obeys a Coulomb potential and its general form is given by<sup>2</sup>

$$\psi_f(r) \underset{r \rightarrow \infty}{=} e^{i\vec{k} \cdot \vec{r}} + f(\hat{r}) \frac{e^{-ikr}}{r}$$

which is the asymptotic form of an incident Coulomb wave plus an incoming spherical wave (see Chapter 3). Then integrating over the delta function in Fermi's Golden rule gives the usual density of states factor

$$\rho = \frac{1}{(2\pi)^3} \frac{mk}{\hbar^2} .$$

Using the unit of length to be the Bohr radius and the unit of energy to be the Rydberg results in

$$\frac{d\sigma}{d\Lambda} = \frac{\alpha}{\pi} \frac{k}{w} |\langle f | \hat{A} \cdot \vec{P} | i \rangle|^2 a_0^2$$

where  $w$  is expressed in Rydbergs. Also it is convenient to use the commutation relation  $[H, P] = i\hbar \nabla V$  resulting in

$$\frac{d\sigma}{d\Lambda} = \frac{\alpha}{\pi} \frac{k}{w} \frac{1}{(\epsilon_f - \epsilon_i)^2} |\langle f | \hat{A} \cdot \nabla V | i \rangle|^2 a_0^2 \quad (2.2)$$

which can be viewed as the one-electron limit<sup>2</sup> of the quadratic response of a system to an external probe. A first principles approach to this problem has been given by

Schaich and Ashcroft<sup>4</sup> and by Caroli et al.<sup>5</sup>

The potential in Equation 2.2 is a one-electron potential. Hermann and Skillman<sup>6</sup> have determined self-consistent potentials which have been used to calculate atomic photoionization cross sections using Hydrogenic wavefunctions.<sup>7</sup> The results have been found to predict the main trends in cross section versus photon energy. See reference 8 for a review of experimental results on atomic cross sections. Also, Hartree-Fock calculations have been performed on some atoms giving cross sections which agree reasonably well with experimental results.<sup>9</sup> But in these early calculations the one electron potential used was that of the ground state. The response of the remaining electrons to the removal of an electron has been neglected. This is valid only in the adiabatic approximation (i.e., the electron is removed slowly) as then the system remains in the ground state and the outgoing electron carries the relaxation energy of the system as kinetic energy. However, if the electron is removed suddenly the ion may be left in various excited states. Discrete states are called shake up lines; shake off satellites are states which include another electron in the continuum.<sup>10</sup> Also core holes may relax by Auger processes or by auto ionization, i.e., the Coulomb repulsion

of electrons acts to de-excite the ion by simultaneously filling the core hole and ejecting a second electron.<sup>11</sup>

In the case of molecules added complications arise due to the vibrational and rotational motions. The rotational levels are neglected because their spacing is about  $.01 \text{ eV}$ <sup>12</sup> and cannot be resolved. The vibrational effects are important only when the Born Oppenheimer approximation (treat the nuclei as fixed and obtain a set of eigenfunctions for fixed nuclei with little coupling between the sets) is no longer valid. The coupling becomes important near level crossings.<sup>13</sup> In this case the matrix element contains both an electron and vibrational term. The Franck-Condon principle<sup>14</sup> states that the initial state vibrational function is sharply peaked about the equilibrium value, so that the electronic term is nearly constant over the integral and the cross section is proportional to the product of the electronic term and the Franck-Condon factor, which is the overlap integral between the initial and final state vibrational functions. We will be dealing with the sum over all final vibrational states so that, if the Franck-Condon principle is valid, all reference to vibrational states drops out. If it is not valid, the cross section represents an average over the initial vibrational state. (Rotational effects are

neglected in our calculations.)

Molecular calculations using plane wave final states have been reported by Ellison and coworkers.<sup>15</sup> Their results do not agree with experimental data for photon energies less than 40 eV. Other calculations reported are those of Schweig and Thiel and coworkers<sup>16</sup>, and others.<sup>17</sup> Tuckwell<sup>18</sup> has gone beyond the plane wave results and calculated cross sections for  $N_2$  and  $O_2$  using a 2 center approximation based on the separability of the Schrodinger equation for a diatomic in prolate spherical coordinates. Similar calculations have been performed on  $H_2$  by Flannery and Öpik<sup>19</sup> and on  $H_2^+$  by Bates and Öpik.<sup>20</sup> In general, for atoms and molecules it has been found that Eq. 2.2 gives cross sections which ordinarily agree with the data to within a factor of 2, except when final states are approximated by a plane wave and then errors an order of magnitude result.

For the case of solids, reviews have been given by Eastman<sup>21</sup> and by Smith<sup>22</sup> who use essentially one electron theories. The short mean free path of electrons far above the Fermi surface limits the photoemission to the surface region. Since it is the electron-electron interactions (inelastic scattering between electrons) which causes the short free path, many body effects should be included from

the start. However, in practice most calculations for solids use the one electron band structure for the bulk and neglect surface and many body effects. The initial and final states are Bloch waves,  $\psi_{\vec{k}}(\vec{r})$ . Liebsch<sup>23</sup> has developed a one electron theory which treats a semi-infinite solid and includes the multiple scattering by the ion cores both for initial and final states. Gadzuk<sup>24</sup> has used multiple scattering theory to treat photoemission from simple molecules adsorbed on solid surfaces which are treated in the tight binding approximation. Strong angular dependences were observed.

For a molecule near a metal surface, screening effects due to the other electrons are particularly pronounced.<sup>25</sup> This may cause substantial local field corrections to the vector potential  $\vec{A}$  of the incident photon<sup>26</sup>, thus decreasing the validity of our neglecting the spatial variation of  $\vec{A}$  and  $\vec{V} \cdot \vec{A}$  term in the Hamiltonian (Eq. 2.1). However, the most dramatic effects on the cross sections are due to the matrix elements themselves, which is what we will calculate in this thesis.

CHAPTER TWO REFERENCES

1. J.J. Sakuri, Advanced Quantum Mechanics (Addison-Wesley, New York, 1967).
2. P.J. Feibelman and D. Eastman, Phys. Rev. B 10, 4932. (1974).
3. H.A. Bethe and E.E. Salpeter, Handbuch der Physik Vol. XXXV (Springer-Verlag, Berlin, 1957).
4. W.L. Schaich and N.W. Ashcroft, Phys. Rev. B 3, 2452 (1971).
5. C. Caroli, D. Lederer-Rozenblatt, B. Roulet and D. Saint-James, Phys. Rev. B 8, 4552 (1973).
6. F. Herman and S. Skillman, Atomic Structure Calculations (Prentice-Hall, Englewood Cliffs, N.J., 1963).
7. J.W. Cooper and S.T. Manson, Phys. Rev. 177, 157 (1969);  
E.J. McGuire, Phys. Rev. 175, 20 (1968);  
F. Combet Farnoux, Journal de Physique 32, C4-7 (1972).
8. J.A.R. Samson, Adv. At. Mol. Phys. 2, 178 (1966).
9. A.F. Starace, S.T. Manson and D.J. Kennedy, Phys. Rev. A9, 2453 (1974).
10. H.W. Meldner and J.P. Perez, Phys. Ref. A4, 1388 (1971);  
J.W. Gadzuk, in "Electronic Structure and Reactivity of Metal Surfaces" NATO Advanced Study Institute Series (Plenum, New York, 1976).

CHAPTER TWO REFERENCES (continued)

11. U. Fano and J.W. Cooper, Rev. Mod. Phys. 40, 441 (1968);  
U. Fano, Phys. Rev. 124, 1866 (1961).
12. D. Dill, Phys. Rev. A6, 160 (1972).
13. M. Born and K. Huang, Dynamical Theory of Crystal Lattices, (Oxford 1954).
14. G. Herzberg, Spectra of Diatomic Molecules (Van Nostrand, N.Y., 1950) p. 199.
15. J.W. Rabalais, T.P. Debies, J.M. Berkosky, J.J. Hunag, and F.O. Ellison, J. Chem. Phys. 61, 516 (1974).
16. M.J.S. Dewar, A. Komornicki, W. Thiel and A. Schweig, Chem. Phys. Letters 31, 286 (1975).
17. I.G. Kaplan and A.P. Markin, Optics and Spectroscopy 24, 475 (1968);  
L.L. Lohr and M.B. Robin, Journ. Am. Chem. Soc. 92, 7241 (1970).
18. H.C. Tuckwell, Journ. Phys. B3, 293 (1970) and Journ. Quant. Spectroscopy and Radiative Transfer 11, 391 (1971).
19. M.R. Flannery and U. Öpik, Proc. Phys. Soc. (London) 86, 491 (1965).
20. D.R. Bates and U. Öpik, Journ. Phys. B1, 543 (1968).

CHAPTER TWO REFERENCES (continued)

21. D.E. Eastman in Techniques of Metals Research. Vol. I  
Pt. 1, E. Passaglia ed. (Interscience, N.Y., 1972)  
p. 411.
22. N. Smith, CRC Crit. Rev. Sol. St. Sci. 2, 45 (1971).
23. A. Liebsch, Phys. Rev. B 13, 544 (1976).
24. J.W. Gadzuk, Phys. Rev. B10, 5030 (1974).
25. E.W. Plummer in Topics in Applied Physics 4, 143  
(1975) (Springer-Verlag, N.Y., 1975);  
P.J. Feibelman, Phys. Rev. B12, 1319 (1975).
26. J.G. Endriz, Phys. Rev. B7, 3463 (1973).



### CHAPTER THREE

#### The SCF- $\chi\alpha$ -SW METHOD

In the SCF- $\chi\alpha$ -SW formalism we are concerned with solving the one electron Schrödinger equation (in Rydberg units)

$$[-\nabla^2 + V(\vec{r})] \psi(\vec{r}) = E\psi(\vec{r}) \quad (3.1)$$

for a local potential function

$$V(\vec{r}) = V_c(\vec{r}) + V_{\chi\alpha}(\vec{r}) \quad (3.2)$$

which includes the coulomb contribution  $V_c(r)$  and the  $\chi\alpha$  statistical density-functional approximation

$$V_{\chi\alpha}(\vec{r}) = -6\alpha[(3/8\pi) \rho(\vec{r})]^{1/3} \quad (3.3)$$

to the exchange effects and removes the electron self-interaction<sup>1</sup> where  $\rho(\vec{r})$  is the electronic charge density. Setting  $\alpha = 1$  gives the exchange potential derived by Slater<sup>2</sup> in 1951, and setting  $\alpha = 2/3$  yields the exchange approximation derived independently by Gaspar<sup>3</sup> and by Kohn and Sham<sup>4</sup>. However, a value for  $\alpha$  chosen systematically between these two limits generally yields more reliable results. Schwarz has systematically determined atomic values of  $\alpha$  by matching the  $\chi\alpha$  total energy of the atom

to the Hartree-Fock total energy.

To solve equation 3.1 for a molecule, one first geometrically partitions the space of the molecule into regions of sufficiently high symmetry such that one dimensional integrals are solutions in each region. The simplest such regions are spheres, centered on each atom with constant potential regions between spheres. This results in three fundamental types of regions:

- I. Atomic: regions within touching spheres centered on the constituent atoms
- II. Interatomic: regions between the atomic spheres and an outer sphere which surrounds the entire molecule
- III. Extramolecular: region exterior to the outer sphere.

The potential  $V_c(r) + V_{\chi\alpha}(\vec{r})$  (eq. 3.2) is then spherically averaged inside each atomic region I and also for region III; it is assumed to be constant throughout region II, equal to the volume average of  $V_c(\vec{r}) + V_{\chi\alpha}(\vec{r})$  over this region. A simple superposition of atomic charge densities is substituted into Poisson's equation to obtain the initial molecular potentials. Because we have partitioned matter into local regions of spherically averaged and volume averaged potentials, we can use a rapidly convergent

partial-wave representation for the solutions of Equation 3.1. We begin by writing down the most general form of these solutions within each region and then match these functions and their derivatives at the sphere boundaries. Once a solution is obtained we must calculate a new potential and iterate to self-consistency.

### 3.1. Solutions for Region I

For region I, inside each atomic sphere  $j$  the wave-functions can be expanded as

$$\psi_j^I(\vec{r}) = \sum(L) C_L^j R_\ell^j(\epsilon, r) Y_L(\vec{r}) \quad (3.4)$$

where  $L = (\ell, m)$  is the partial wave angular momentum index. The  $Y_L(r)$ 's are the spherical harmonics, the  $C_L^j$  coefficients are to be determined, and the  $R_\ell^j(\epsilon, r)$  are the solutions of the radial Schrodinger equation

$$\left[ -\frac{1}{r^2} \frac{d}{dr} r^2 \frac{d}{dr} + \frac{\ell(\ell+1)}{r^2} + V^j(r) - \epsilon \right] R_\ell^j(\epsilon, r) = 0 \quad (3.5)$$

The potential near the origin  $r = 0$  will be dominated by the coulomb attraction at the nucleus which is given by

$$V(r) = -2z/r$$

$r \rightarrow 0$

where  $z$  is the atomic number. The solutions in this region will then be the regular coulomb functions. They must be

finite at the origin and are generated by outward numerical integration of equation (3.5) for each partial wave component and each trial energy. This form applies for both bound and continuum states.

### 3.2. Solutions for Region III

In the extramolecular region III, we must allow for both the regular and irregular solutions so that

$$\psi^{\text{III}}(r) = \Sigma(L) [C_L^O R_L^O(\epsilon, r) + B_L^O g_L^O(r)] Y_L(r). \quad (3.6)$$

For bound states ( $\epsilon < 0$ ) we choose  $C^O = 0$  and then  $g_L^O$  is the linear combination of coulomb functions which decays exponentially for large  $r$ , satisfying the potential for large  $r$  which is also coulombic. For the unbound states  $R_L^O(\epsilon, r)$  and  $g_L^O(r)$  are proportional to the regular and irregular coulomb wave functions which are solutions to the differential equation

$$[\nabla^2 + k^2 - \frac{2\gamma k}{r}] \psi(\vec{r}) = 0 \quad (3.7)$$

where  $k^2 = \epsilon$  and  $\gamma = \frac{Z_1 Z_2}{k}$ . For an electron  $z = -1$ .

The most general form of the solution is

$$\psi(\vec{r}) = \frac{y_L(r)}{r} Y_L(\vec{r}).$$

Inserting this solution into equation 3.7 yields

$$\left[ \frac{d^2}{dr^2} + k^2 - \frac{2\gamma k}{r} - \frac{\ell(\ell+1)}{r^2} \right] Y_\ell(r) = 0 \quad (3.8)$$

The solutions are the regular solution  $F_\ell(\gamma, \rho)$  and the irregular solution  $G_\ell(\gamma, \rho)$  where  $\rho = kr$ .

Thus the solutions  $R_\ell^O(\varepsilon, r)$  and  $g_\ell^O(r)$  given above are equal to  $\frac{F_\ell(\gamma, \rho)}{kr}$  and  $-\frac{G_\ell(\gamma, \rho)}{kr}$  respectively. The asymptotic forms of these functions are

$$F_\ell(\gamma, \rho) \underset{r \rightarrow \infty}{=} \sin \left[ kr - \frac{\ell\pi}{2} \gamma \ln 2kr + \sigma_\ell \right]$$

$$G_\ell(\gamma, \rho) \underset{r \rightarrow \infty}{=} \cos \left[ kr - \frac{\ell\pi}{2} \gamma \ln 2kr + \sigma_\ell \right]$$

where  $\sigma_\ell$  is the phase shift defined by

$$\sigma_\ell = \text{Arg } \Gamma(\ell + 1 + i\gamma)$$

and the full expansion of the coulomb wave is

$$\psi_c^\pm(r) = \sum(L) 4\pi i^{-L} e^{\pm i\sigma_\ell} \frac{F_\ell(\gamma, \rho)}{kr} Y_L(r) Y_L^*(k) \quad (3.9)$$

(See ref. 6).

### 3.3 Solutions for Region II.

For the intersphere region II, the Schrödinger equation becomes

$$(\nabla^2 + \varepsilon - \bar{V}_{II}) \psi^{II}(\vec{r}) = 0$$

where  $\bar{V}_{II}$  is the volume average of  $V_c(r) + V_{\chi\alpha}(r)$  over that

region. The solutions are linear combinations of spherical Bessel functions obtained by substitution of Green's function (defined by  $(\nabla^2 + k^2) G(\vec{r}, \vec{r}') = \delta(\vec{r} - \vec{r}')$ ) into Green's theorem. Employing the spherical harmonic expansion of Green's function

$$G(\vec{r}, \vec{r}') = \frac{\cos|\vec{r} - \vec{r}'|}{|\vec{r} - \vec{r}'|} = -k \sum_L j_\ell(kr_<) n_\ell(kr_>) Y_L^*(\hat{r}) Y_L(\hat{r}')$$

where  $r_>$  and  $r_<$  are the greater and lesser of  $r$  and  $r'$  (see ref 6,7) results in

$$\begin{aligned} \psi^{II}(r) = & \sum(L) i^{-L} A_L^0 j_L(ikr_0) Y_L(r_0) \\ & - \sum(j) \sum(L) i^{-L} A_L j_L^{(1)}(ikr_j) Y_L(r_j) \end{aligned} \quad (3.10)$$

for  $\epsilon < \bar{V}_{II}$  and for  $\epsilon > \bar{V}_{II}$  as

$$\psi^{II}(r) = \sum(L) A_L^0 j_L(ikr_0) Y_L(r_0) + \sum(j) \sum(L) A_L j_L^{(1)}(ikr_j) Y_L(r_j) \quad (3.11)$$

where  $j_\ell(ikr_0)$  is a spherical Bessel function,  $h_\ell^{(1)}(ikr_j)$  is a spherical Hankel function of the first kind, and  $n_\ell(ikr_j)$  is a spherical Neumann function. The first term in expressions 3.10 and 3.11 may be thought of as a superposition of "incoming" spherical waves, which have been scattered by the potential of region III. The second term may be

interpreted as a superposition of "outgoing" spherical waves, which have been scattered by the potential of the atomic regions I.

### 3.4. Total Solutions

Next we match these functions and their derivatives at each sphere boundary. This can be accomplished by transforming products of spherical Bessel functions and spherical harmonics from one site to another by use of the general theorem<sup>8</sup>

$$h_{\ell}(kr) Y_L(\vec{r}) = \sum_{L', L''} 4\pi i^{\ell' + \ell'' - \ell} I(L, L', L'') \quad (3.12)$$

$$h_{\ell}(kr_>) j_{\ell''}(kr_<) Y_{L'}(\vec{r}_1) Y_{L''}(\vec{r}_2)$$

where  $r = r_1 + r_2$  and  $r_>$  and  $r_<$  the greater and lesser of these two.  $h_{\ell}$  is any spherical Bessel function and  $I$  is the Gaunt integral given by

$$I(L, L', L'') = \int Y_L^*(\vec{r}) Y_{L'}(\vec{r}) Y_{L''}(\vec{r}) d\Lambda \quad (3.13)$$

It can also be written as

$$I(L, L', L'') = \left[ \frac{(2\ell' + 1)(2\ell'' + 1)}{4\pi(2\ell + 1)} \right]^{\frac{1}{2}} C(\ell', \ell'', \ell; m', m'', m) \quad (3.14)$$

$$C(\ell' \ell'' \ell; 0 0 0)$$

where the C's are the Clesbsch-Gordon coefficients.<sup>9</sup>

The resulting set of equations can be written as<sup>7</sup>

$$\sum (j) (L') G_{LL'}^{ij} A_{L'}^j = \left[ \frac{g_{\ell}^R}{g_{\ell}^n} \right] C_L^i \delta_{i0} \quad (3.15)$$

For bound states  $C_L^0 = 0$  and we have a homogeneous system of equations in  $N \times L$  unknowns, where  $N$  is the number of spheres and  $L$  the number of partial waves per sphere.

For the continuum states we have an inhomogeneous system since any energy is allowed. The solution to the inhomogeneous system is a linear combination of the corresponding homogeneous solution and any inhomogeneous solution. To find an inhomogeneous solution we must solve the multiple scattering Equations (3.15) with  $C_L^0 = \delta_{L\Lambda}$ . This defines the rows of the real symmetric  $K$  matrix, which is diagonal for spherical potentials. Rewriting the solution of the homogeneous system to incorporate the  $K$  matrix gives<sup>7</sup>

$$\psi_{\Lambda}(\vec{r}) = R_{\Lambda}^0(r_0) Y_{\Lambda}(\hat{r}_0) + \sum (L) K_{\Lambda L} g_{\ell}^0(r_0) Y_L(\hat{r}_0).$$

We may then take the general solution to be

$$\psi(\vec{r}) = \sum (\Lambda) \alpha_{\Lambda} \psi_{\Lambda}(\vec{r}) \text{ or using asymptotic}$$

forms

$$\psi(\vec{r}) \sim \sum (\Lambda) \sum (L) \alpha_{\Lambda} [\delta_{\Lambda L} \sin \theta_{\ell} - i k_{\Lambda L} \cos \theta_{\ell}] Y_L(\vec{r}) \quad (3.16)$$



where

$$\theta_{\ell} = kr - \ell\pi/2 - \gamma \ln 2kr + \sigma_{\ell}.$$

Matching the outgoing wave part of Equation 3.16 with that of the coulomb wave (Eq. 3.9) results in

$$a_{\Lambda} = \sum(L) 4\pi i^{\ell} e^{-i\sigma_{\ell}} Y_{\Lambda}^{*}(\hat{k}) (1-ik)^{-1}_{\Lambda\Lambda} \quad (3.17)$$

Then for the outer sphere we may write

$$\begin{aligned} \psi(\vec{r}) = \sum(L) \sum(L') 4\pi i^{\ell} e^{-i\sigma_{\ell}} Y_{\Lambda}^{*}(\hat{k}) Y_{\Lambda'}(\hat{r}) \left[ \left( \frac{1}{1-ik} \right)_{\Lambda\Lambda'} f_{\ell}(r) \right. \\ \left. + \left( \frac{1}{1-ik} \right)_{\Lambda\Lambda'} g_{\ell}(r) \right] \end{aligned} \quad (3.18)$$

$$\text{where } \left( \frac{1}{1-ik} \right)_{\Lambda\Lambda'} = \sum_{\Lambda} (1-ik)^{-1}_{\Lambda\Lambda} \delta_{\Lambda\Lambda'}$$

For the atomic sphere we have

$$\psi(\vec{r}_i) = \sum(L) \sum(L') 4\pi i^{\ell} e^{-i\sigma_{\ell}} Y_{\Lambda}^{*}(\hat{k}) Y_{\Lambda'}(\hat{r}_i) \left( \frac{A^i}{1-ik} \right)_{\Lambda\Lambda'} f_{\ell}(r_i) \quad (3.19)$$

$$\text{where } \left( \frac{A^i}{1-ik} \right)_{\Lambda\Lambda'} = \sum_{\Lambda} (1-ik)^{-1}_{\Lambda\Lambda} A^i_{\Lambda\Lambda'}$$

### 3.5. Matrix Elements

In order to calculate the matrix elements for the photoionization process, consider an atomic sphere for which

the initial state can be written (Eq. 4)

$$\psi_j(\vec{r}) = \sum (L) C_L^j R_\ell^j(r_j) Y_L(\vec{r})$$

and the final state is given above (eq. 3.19).

The interaction is proportional to

$$\hat{A} \cdot \nabla V = \hat{A} \cdot \hat{e}_r \partial V / \partial r$$

but

$$\hat{A} \cdot \hat{e}_r = \sum_v \frac{4}{3} \pi Y_{\ell v}^*(\hat{A}) Y_{\ell v}(\hat{r}) \quad (3.20)$$

so for an atomic sphere  $j$  the matrix element is

$$M^j = \sum_{vLL',L''} \frac{(4\pi)^2}{3} (-i)^\ell e^{i\sigma_\ell} \left( \frac{A^j}{1-ik} \right)_{LL'} \hat{A}_{L''}^j Y_L(\hat{k}) \\ Y_{0v}^*(\hat{A}) R_{\ell, \ell''}^j I(L', 0v, L'') \quad (3.21)$$

Here  $I$  is the Gaunt integral and

$$R_{\ell, \ell''}^j = \int_{\text{sphere}} r_j^2 dr_j f_{\ell, \ell''}^j(r_j) \frac{\partial V}{\partial r_j} f_{\ell''}^j(r_j)$$

Equation 3.21 can be rewritten as

$$M^j = \sum (L) (v) \frac{4\pi}{3} Y_{0v}^*(\hat{A}) F^j(L, v) Y_L(\hat{k}). \quad (3.22)$$

The outer sphere matrix element has the same form as Eq. 3.22, the intersphere region with  $\frac{\partial V}{\partial r} = 0$  makes no contribution, and thus the full matrix element is given by

$$M = \sum (L)(\nu) \frac{1}{3} Y_{0\nu}^*(\hat{k}) F(L, \nu) Y_L(\hat{k}) \quad (3.23)$$

which defines  $F$ .

For the total cross section values the matrix element must be averaged over all orientations. Thus we take the absolute square of  $M$  (Eq. 3.23) and integrate over all  $\hat{k}$  and average over all directions  $\hat{A}$ . (See Ref. 7). This results in

$$\sigma = \frac{\alpha}{\pi} \frac{k}{\omega} \frac{1}{(\epsilon_f - \epsilon_i)^2} \frac{4\pi}{9} \sum_{L, \nu} |F(L, \nu)|^2 \quad (3.24)$$

which is the angle averaged or total cross section for photoemission measurements (done without angular resolution).

CHAPTER THREE REFERENCES

1. J.C. Slater, Quantum Theory of Molecules and Solids, Vol. 4 (New York, McGraw-Hill, 1974), p. 583.
2. J.C. Slater, Phys. Rev. 81, 385 (1951).
3. R. Gaspar, Acta. Phys. Acad. Sci. Hung. 3, 263 (1954).
4. W. Kohn, L.J. Sham, Phys. Rev. A140, 1133 (1965).
5. K. Schwarz, Phys. Rev. B5, 2466 (1972).
6. A. Messiah, Quantum Mechanic (Wiley, N.Y. 1966).
7. J.W. Davenport, Dissertation, University of Pennsylvania, Philadelphia, Pa. 1976.
8. K.H. Johnson, Adv. Quan. Chem. 7, 143 (1973).
9. M.E. Rose, Elementary Theory of Angular Momentum (Wiley, N.Y., 1957).

## CHAPTER FOUR

### PREVIOUS ZNO STUDIES

#### 4.1. Photoemission

Both Xray and UV photoemission (XPS and UPS) measurements on semiconductor ZnO have been reported in the literature. In general, the experiment consists of irradiating the sample (single crystals are used to avoid grain boundary problems) with monoenergetic radiation ( $\hbar\omega$ ) and measuring the kinetic energies ( $E_k$ ) of the photoemitted electrons. Then using the relation

$$E_k = \hbar\omega - E_b \quad (\text{Eq. 1.1})$$

the binding energies ( $E_b$ ) of the emitted electrons can be determined. These binding energies correspond to the electronic states of the solid. The number of electrons leaving the solid with a given kinetic energy is a measure of the cross section of that particular state at the given photon energy. In the more familiar case of gases, the states are usually sufficiently far apart in energy such that a cross section peak can be resolved for each state. For solids, the energy levels are closely spaced in bands permitting resolution of only a few peaks which represent cross section contributions from

all the different states.

Implicit in Eq. 1.1 is the assumption that all electrons leaving a particular orbital arrive at the detector with the same kinetic energy, obviously not the case for a real solid. Other factors arise to complicate the picture. One of the largest and most complicating factors is the energy loss of the emitted electrons on their way out of the solid due to inelastic scattering. Also the relaxation effects of the system due to the absence of the emitted electron, the natural line broadening due to the lifetime of the ionized state, and thermal broadening produce an uncertainty in the deduced value of the binding energy,  $E_b$ .

#### 4.1.1. Experimental Uncertainties

Of course other uncertainties are introduced by the actual experimental setup and procedure used. Some uncertainties are common to all photoemission spectrometers. The resolution of the spectrometer is defined as the smallest energy difference between two groups of electrons that will result in separate photoelectron bands in the spectrum. This is usually estimated by using the full width at half maximum intensity (FWHM) recorded when the true line shape is theoretically known. The spectra

exhibit considerable random fluctuations and statistical noise due to the low electron count rates. Thus the intensities have an uncertainty equal to the square root of the total number of electrons counted at a given voltage. Also, photoemission band intensities are a function of the intensity of the incident radiation, slit widths, the type of energy analyzer, and surface charges on the walls of the analyzer chamber and slits. For a given spectrometer, these parameters can be kept more or less constant; however, comparisons of spectra from different experimental setups should be made with caution. Even for a given spectrometer, large distortions of the intensities may arise due to the discrimination of the analyzer for electrons of different energy.<sup>1</sup> The sum of the contributions to the uncertainty tend to broaden structure seen in the measured spectra and shift it to lower energies.<sup>11</sup>

#### 4.1.2. Spectrometer Transmission and Broadening

In order to extract meaningful cross section values from recorded spectra, it is necessary to understand the transmission and broadening characteristics of the spectrometer. A spectrometer's broadening function is equivalent to the energy distribution curve (EDC) that

would be measured if the true distribution were a delta function of monoenergetic electrons. Of course the shape of the broadening or response function can only be guessed. Its width can be estimated from the total of the contributions to resolution errors due to the experimental equipment. A measure of the response function width can be obtained from an EDC of a metal, since theoretically in the absence of broadening, the high energy cutoff is determined by the Fermi distribution function. Also depending on the type of energy analyzer used, the width of the response function may or may not be constant.

The broadening effect of the spectrometer on the measured EDC can be expressed by the relation

$$O(E') = \int R(E-E') I(E) dE \quad (4.1)$$

where  $O(E')$  is the recorded EDC,  $R(E-E')$  is the instrumental response function, and  $I(E)$  is the true spectrum seen by the detector.

The transmission characteristics of the spectrometer determine the measured intensity of the EDC. To obtain an absolute or normalized EDC, the ordinate must be scaled properly. Since the ordinate (intensity) of an EDC is given in terms of electrons per absorbed photon



per eV, it is necessary to know the quantum yield, i.e., the efficiency with which the incident photons produce photoelectrons. The absolute quantum yield is defined as the ratio of the number of electrons emitted to the number of absorbed photons. The number of absorbed photons is determined by the incident photon flux, the transmission of any windows and/or grids the light must go through, and by the reflectivity of the sample. These values must be determined from separate measurements.

#### 4.1.3. Work Function and Threshold

The work function and photoelectric threshold generally do not coincide for a semiconductor. The photoelectric threshold is defined as the energy from the valence band maximum (top of the valence band) to the vacuum level or equivalently the energy gap plus the electron affinity. Several factors make the determination of the threshold from yield data difficult. First, band structure effects and optical selection rules often appear to play an important part in photoemission from semiconductors. Another complexity is that produced by band bending, which complicates the curve near threshold. A third factor is the possibility of photoemission from impurities in the forbidden gap as well as from surface states.

The photoelectric threshold is important in determining the Fermi level of the sample.

$$E_F = \phi_E - E_a = \phi_C - V_{cpo} - E_a \quad (4.2)$$

where  $\phi_E$  is the work function of the sample,  $\phi_C$  is that of the collector can,  $E_a$  is the electron affinity of the sample and  $V_{cpo}$  is the contact potential between the collector and emitter. If the band-bending region is small compared to the escape depth of the electrons, the value of  $E_F$  obtained will apply to bands in the bulk. If the region is larger compared to the escape depth, the value of  $E_F$  obtained will correspond to bands at the surface. If the region is comparable to the escape depth,  $E_F$  might appear to be a function of the photon energy and will not be well defined.<sup>2</sup> In order to circumvent this problem, measurements are given with respect to the valence band maximum (VBM).

#### 4.1.4. Ultra High Vacuum Requirements

The "zero of potential" to which the electron energy is referred is actually the work function of the collector can. It is important to carry out photoemission measurements in ultra high vacuum because contaminated surfaces

usually have a wide variation in work function. If the work function of the sample holder or that of the sides of the sample is higher than the sample work function, fringing emitter fields produce a potential barrier in front of the emitter which distorts the low energy part of the EDC such that it is shifted to lower energies and broadened.<sup>10</sup> Nonuniformity of the work function on the actual emitting surface also distorts the low energy part of the EDC.

#### 4.2. ZnO Photoemission Experimental Studies

The most complete UV photoemission study of ZnO has been reported by Powell, et al.<sup>3</sup>. Measurements were made for photon energies between 7.8 and 11.6 eV at pressures less than  $10^{-10}$  Torr employing the ac retarding method. Additional measurements were made for 11.6 to 21.2 eV in pressures of about  $10^{-4}$  Torr. The ultra high vacuum curves are reproduced in Chapter Five for comparison with results from this work. Since the experimentalists were able to normalize their EDC's, an intensity comparison between the theoretical and experimental results is made in Section 5.6. Important features reported, deduced from the EDC's are the location of the Zn3d band at  $7.5 \pm 0.2$  eV below the VBM

and the width of the upper valence band, which appears to be about 5 eV. Also, with respect to the top of the valence band, maxima in the conduction band density of states were found at  $8.5 \pm 0.2$  eV and  $10.4 \pm 0.2$  eV, while two valence band maxima were found at  $-1.6 \pm 0.2$  and  $-2.8 \pm 0.2$  eV.

X-ray photoemission measurements have been done by Ley et al.<sup>4</sup>. The AlK $\alpha$  photon source of 1486.6 eV was used in pressures of about  $10^{-8}$  Torr. These curves are reproduced in Chapter Five for comparison to our curves. Important band features deduced from the measurements are the location and width of the 3d band 8.8 eV below the VBM and 2 eV, respectively. The upper valence band width is reported about 7 eV and the O<sub>2s</sub> nonbonding peak is at -20.7 with respect to the VBM. All values are reported with uncertainties of  $\pm 0.1$  eV.

Earlier UV and X-ray measurements reported by Vesely et al.<sup>5</sup> placed the Zn3d location at  $8.5 \pm 0.4$  eV and  $8.6 \pm 0.2$  eV below the VBM. All these values are summarized and compared to our calculated values in Table 5.1. (See Chapter Five). However, we are mainly concerned with a comparison between the XPS results of Ley et al.,<sup>4</sup> the UPS results of Powell et al.,<sup>3</sup> and our results. We present the others in Table 5.1 as evidence

of the reproducibility of the experimental results.

#### 4.3. Optical Experimental Studies

Also electron energy loss and ultraviolet reflectivity spectra of ZnO have been reported by Hengehold et al.<sup>6</sup> These spectra are shown in Figures 4.2(a) and 4.2(b). The reflectivity measurements (which show strong peaks near regions of interband transitions) exhibit structure at 3.3, 5.0, 7.3 and 8.4 eV and in the 11-16 eV region. If we assume this last structure is due to the transition of electrons in the valence band to the conduction band maxima at  $8.5 \pm 0.2$  eV and  $10.4 \pm 0.2$  eV above the VBM (UPS results), this leads to a valence band of approximately 4.6 eV. The energy loss curve on the other hand exhibits a large peak at the plasma excitation energy while the interband transitions are considerably diminished in size. The energy loss measurements yielded peaks at 3.8, 5.5, 9.5, 13.5, 18.8 and 35.5 eV. The dominant peak is the 18.8 eV one and has been attributed to a plasma excitation. This plasmon excitation is seen in the XPS data in Section 5.5.

#### 4.4 Theoretical Studies

Rössler<sup>7</sup> has used the Korringa-Kohn-Rostoker

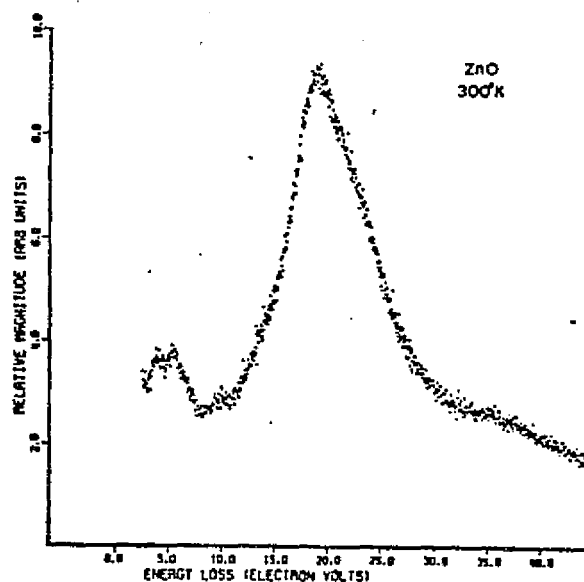


Figure 4.2(a). Energy-loss spectrum of a typical ZnO platelet, Ref. 6.

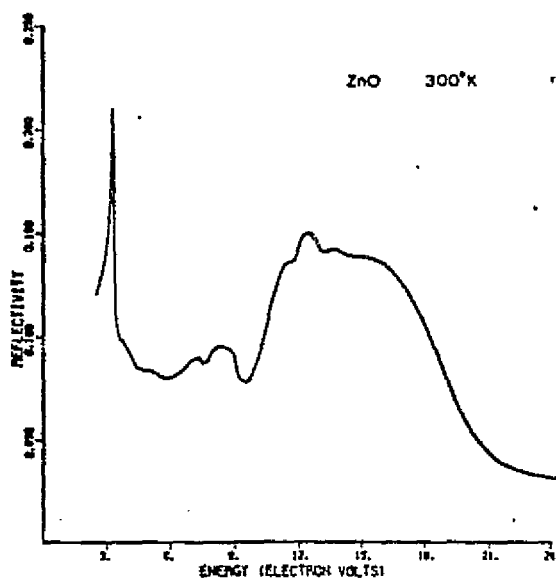


Figure 4.2(b). Near-normal incidence reflectivity spectrum typical of a platelet of ZnO at 300°K. Ref. 6.

(KKR) method to calculate a band structure for zinc oxide. The resultant band structure is shown in Figure 4.3(a). This method involves the use of an ad hoc potential with only a single parameter which is adjusted to obtain the correct band gap. From Figure 4.3(a) it can be seen that ZnO exhibits a broad free electron-like lowest conduction band about 1.6 eV wide, Zn3d levels lying closely below the upper valence bands and p-antibonding conduction band states 17 eV above the top of the valence band. The KKR calculation is in good agreement with the experimental photoemission results except for the location of the Zn3d state and the width of the upper valence band. The calculation predicts 4 eV and 3.5 eV respectively, while experimentally the values are in the ranges of 7.5 to 8.5 eV and 5.0 eV.

A pseudopotential band structure calculation has been carried out by Bloom and Ortenburger.<sup>8</sup> In pseudopotential theory, a local repulsive potential is constructed that cancels the crystal potential in the core region resulting in a smooth pseudopotential. Such a calculation does not include the Zn3d bands at all, which may be justifiable if these bands lie deep enough such that their effect on the valence bands is negligible. As with the KKR calculation, the pseudo-

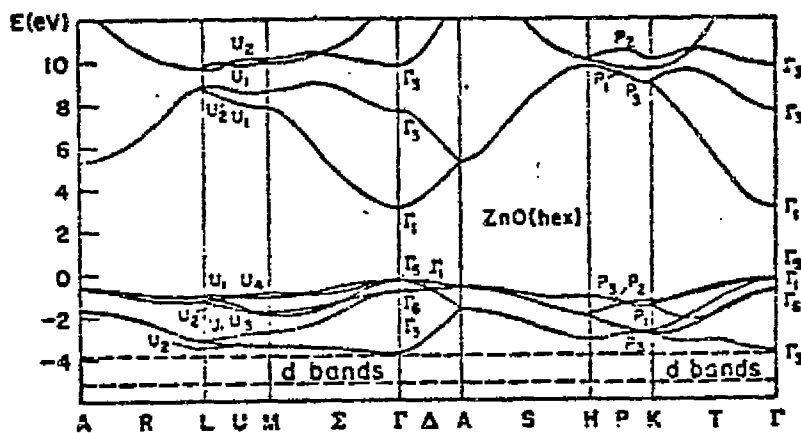


Figure 4.3(a). Energy bands of hexagonal ZnO.  
KKR method. Ref. 7.

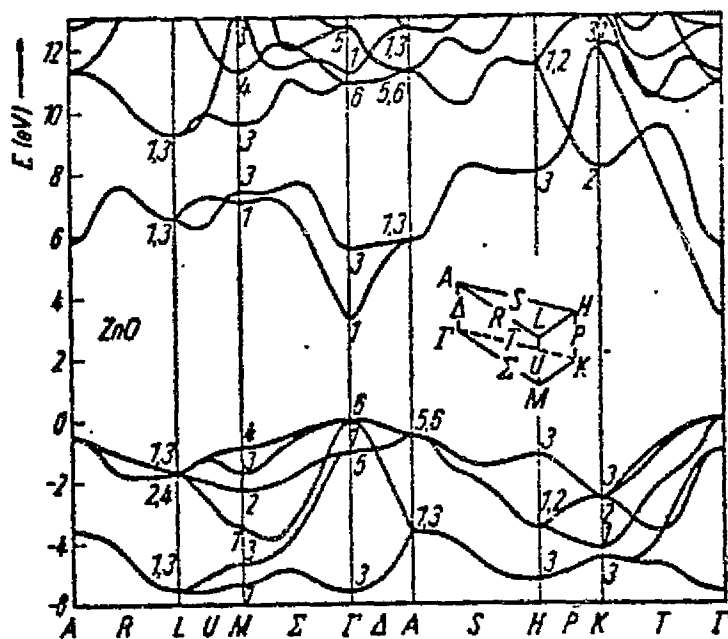


Figure 4.3(b). Energy bands of hexagonal ZnO.  
Pseudopotential method. Ref. 8.

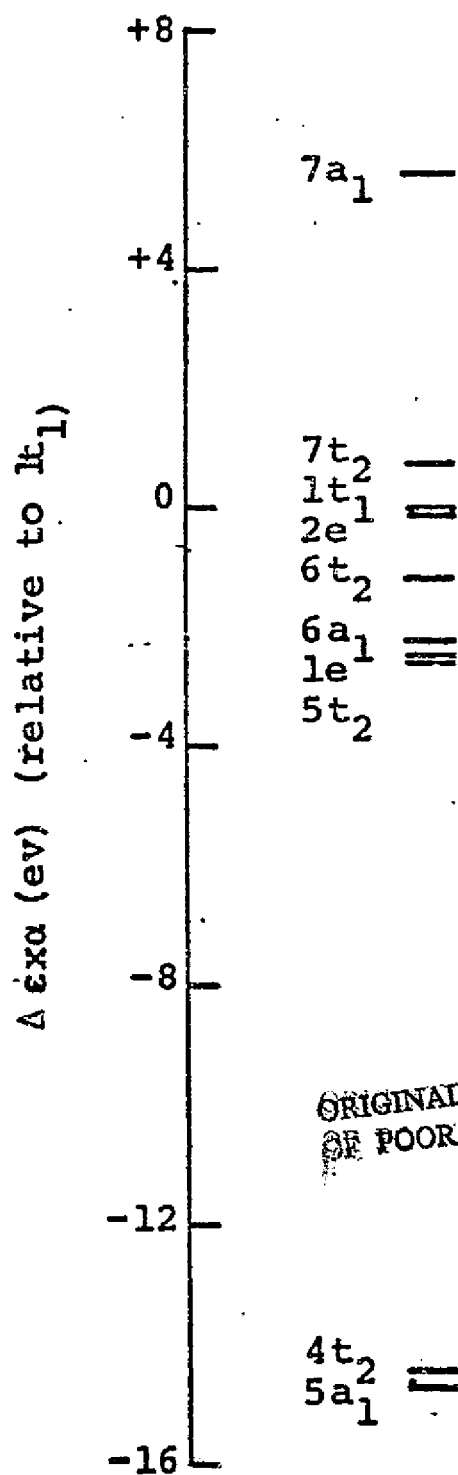


potential calculation seems to be in general agreement with the experimentally determined values. The band diagram is shown in Figure 4.3(b).

SCF- $\gamma\alpha$ -SW calculations have been carried out on ZnO by Tossel.<sup>9</sup> The MO diagram for the cluster model used ( $\text{ZnO}_4^{-6}$ ) is shown in Figure 4.4. The diagram shows a set  $\text{O}_{2s}$  nonbonding orbitals ( $5a_1, 4t_2$ ), two  $\text{Zn}4s, 4p$ - $\text{O}2p$  bonding orbitals ( $6a_1, 6t_2$ ), a set of  $\text{Zn}3d$ - $\text{O}2p$  bonding orbitals ( $1e, 5t_2$ ) and a set of essentially nonbonding  $\text{O}2p$  orbitals ( $2e, 1t_1, 7t_2$ ). The lowest empty orbital is the  $7a_1$  level of the conductive bands, of  $\text{Zn}$ - $\text{O}2p$  antibonding character. Thus the  $\text{Zn}3d$  orbitals are predicted to be about 4 eV below the top of the valence band, some 3.5 eV higher than that predicted by the UPS. However, a transition state calculation was performed on the  $\text{Zn}3d$ -like level ( $1e$ ). This consists of removing one-half of an electron from the particular level and then solving the one electron Schrödinger equation until self consistency is obtained. The idea behind the transition state concept is to represent the initial state and the one-electron potential in the photoemission process more realistically, i.e., include relaxation effects, than with the ground state. In the transition state calculation the  $1e$  energy is lowered by 3.2 eV,

bringing it into much better agreement with the UPS results. This large shift in energy is reasonable since the Zn3d level is localized and the removal of one-half of an electron represents a large relaxation effect on that level. Thus the transition state calculations of the cluster approach represent the photoemission initial states much more accurately than the band calculations.

Figure 4.4. Molecular Orbital diagram of hexagonal ZnO, SCF- $\chi\alpha$ -SW method. Ref. 9.



CHAPTER FOUR REFERENCES

1. J.W. Rabalais, Principles of Ultraviolet Photoelectron Spectroscopy, John Wiley Sons, New York (1977).
2. G.F. Derbenwick, D.T. Pierce, and W.E. Spicer, in Methods of Experimental Physics, Academic Press, New York, edited by R.V. Coleman (1974).
3. R.A. Powell, W.E. Spicer, and J.C. McMenamin, Phys. Rev. B 6, 3056 (1972).
4. L. Ley, R.A. Pollak, F.R. McFeely, S.P. Kowalczyk, and D.A. Shirley, Phys. Rev. B 9, 600 (1974).
5. C.J. Vesely, R.L. Hengehold, and D.W. Langer, Phys. Rev. B 5, 2296 (1972); also C.J. Vesely, and D.W. Langer, Phys. Rev. B 4, 451 (1971).
6. R.L. Hengehold, R.J. Almassy, and F.L. Pedrotti, Phys. Rev. B 1, 4784 (1970).
7. U. Rössler, Phys. Rev. 184, 733 (1969).
8. S. Bloom and I. Ortenburger, Phys. Stat. Sol. (b) 58, 561 (1973).
9. J.A. Tossel, Chem. Phys. 15, 303 (1976).
10. T.H. DiStefano and D.T. Pierce, Rev. Sci. Instrum. 41, 180 (1970).
11. D.T. Pierce, Ph.D. Dissertation, Stanford Univ. (1970).

## CHAPTER FIVE

### PRESENT STUDY

#### 5.1. Choice of Parameters

Photoemission cross section calculations were carried out for the ground state orbitals of wurtzite ZnO. The model used was four oxygen ions in the tetrahedral coordination with a zinc atom in the center. Each oxygen ion carried 9.5 electrons, resulting in the oxyanion  $\text{ZnO}_4^{-6}$ . In consideration of the surface sensitivity of photoemission, this cluster was chosen since it represents a "building block" of a ZnO surface, which like the bulk, has the wurtzite structure (see Figure 5.1).

For the calculations the surface Zn-O bonding distance of  $1.99\text{\AA}$  was used, and the nonoverlapping sphere radii used were as follows:

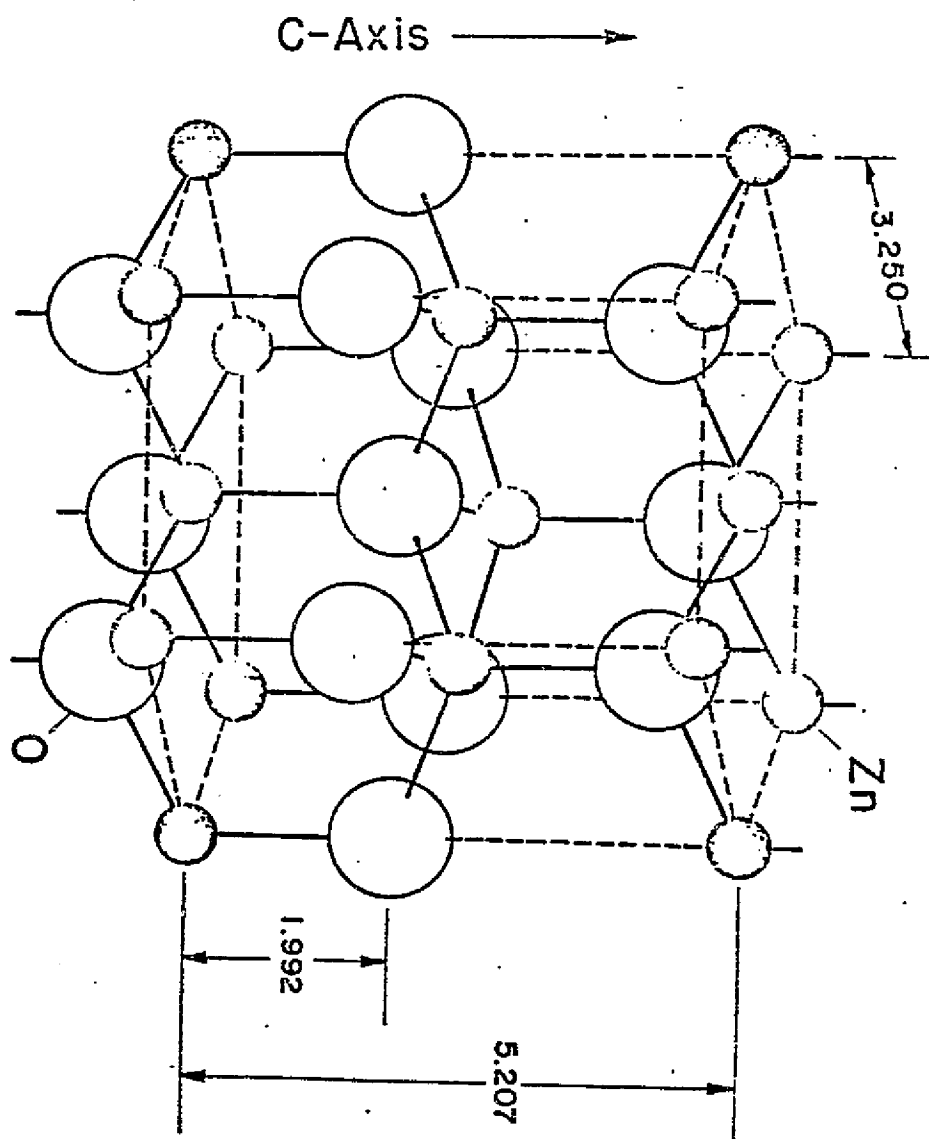
$$r(\text{OUT}) = 5.40 \text{ a.u. (atomic units)}$$

$$r(\text{Zn}) = 2.12 \text{ a.u.}$$

$$r(\text{OXY}) = 1.64 \text{ a.u.}$$

the statistical scaling parameter  $\alpha$  was chosen to be .74447 in the oxygen spheres, .70677 in the zinc sphere, and .72623 in the intersphere and outer sphere regions.

Figure 5.1. Surface structure of wurtzite ZnO. Ref. 1.



These values were taken from Schwarz.<sup>2</sup>

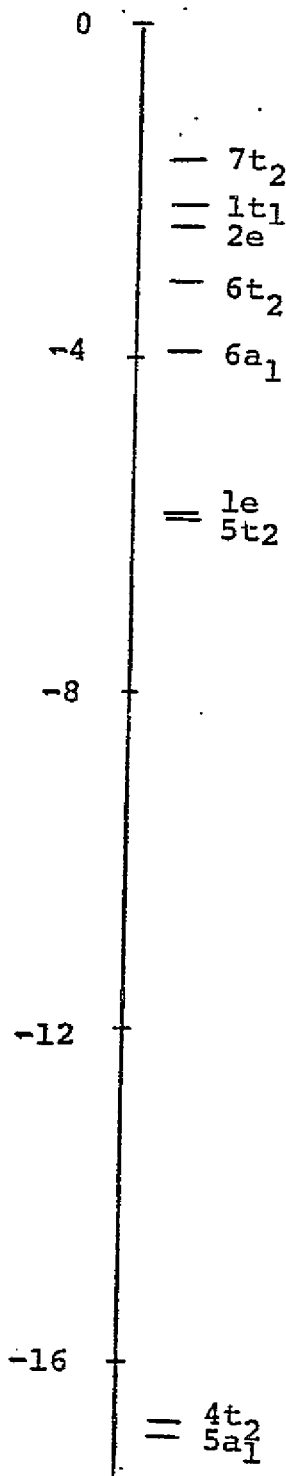
In calculating the photoemission cross sections, the highest energy occupied level ( $7t_2$ ) was used to represent the top of the valence band. The ionization potential for this level was set to 5.0 eV (assuming a collector work function of 5.0 eV reported by UPS) and the rest were scaled accordingly.

## 5.2. Orbital Structure of ZnO

The calculated SCF- $\chi_\alpha$ -SW molecular orbital (MO) diagram for the ground state of the  $\text{ZnO}_4^{-6}$  cluster is shown in Figure 5.2. Our results are in good agreement with Tossels'  $\chi_\alpha$  calculations (see Section 4.4) using somewhat different sphere radii. Figure 5.2 shows a set of  $\text{O}_{2s}$  nonbonding orbitals ( $5a$ ,  $4t_2$ ), a set of  $\text{Zn}3d$ - $\text{O}2p$  bonding orbitals ( $1e$ ,  $5t_2$ ), two  $\text{Zn}4s$ ,  $4p$ - $\text{O}2p$  bonding orbitals ( $6a_1$ ,  $6t_2$ ), and a set of nonbonding  $\text{O}2p$  orbitals ( $2e$ ,  $1t_1$ ,  $7t_2$ ).

Since our final goal is to compare the calculated photoemission cross sections with the experimental data, it is important to understand the differences between the calculated structure and that deduced experimentally, and even more important to understand the role of the orbital structure in dictating the observed spectra. In comparing the calculated structure with the experimental structure,

Figure 5.2. Molecular orbital diagram for ground state energies of  $\text{ZnO}_4^{6-}$ . Energies are in eV and given with respect to the VBM. We have lined up our first state ( $7t_2$ ) with that of the UPS results. (See Table 5.1)





one must remember that the MO diagram represents the ground state, whereas the experimental data represents a perturbed state. While it is not clear exactly how to describe this perturbed state, it is probably somewhere between the ground state and the transition state.

In the remainder of this section we will compare our calculated structure with the experimental observations. At the end of this section we present a summary of these findings in Table 5.1.

#### 5.2.1. Comparison of Theoretical and Experimental Orbital Structure

Quite often in the comparison of theoretical orbital structure with experimental data, an empirical attempt is made to broaden the calculated discrete levels into the observed bands. This procedure may be thought of as simulating the effect of adding more shells of atoms to the cluster in order to compensate for the finite size of the cluster. The usual procedure is to center a Gaussian on each of the discrete levels, whose height is equal to the occupancy of that state and the broadening factor is an adjustable parameter.<sup>3</sup> While the occupancy of the initial state is a factor in the calculation of the intensity, the matrix element for the probability of a

transition is by far the most dominant factor, thus this empirical broadening technique cannot account at all for the observed intensities. However, a correlation between the calculated energy levels and the experimental band energies may be possible enabling identification of the initial states responsible for a given observed band.

An examination of our calculated energy levels (Figure 5.2) shows four groups of levels, and indeed the XPS (see Section 4.2) results resolves four peaks. However, closer examination of the first two groups which compromise the upper valence band (states  $7t_2$ ,  $1t_1$ ,  $2e$ ,  $6t_2$ , and  $6a_1$ ) reveals a band width of 2.3 eV, while both the UPS and XPS results give higher values, approximately 5 and 7 eV respectively. From Table 5.1 it can be seen that this same discrepancy holds for the widths of the  $Zn3d$  levels and the  $O_{2s}$  levels, so that our predicted band widths are too small.

Using the VBM as our reference zero, comparison of the locations of the UPS peaks and the XPS peaks in Table 5.1 generally results in nonagreement between the two values. One explanation for the experimental discrepancies is the extreme instrumental sensitivity to stray surface charges and impurities in determining the zero reference as discussed in Sections 4.13 and 4.14. However, a

the deeper lying band structure more closely resembles that deduced from the XPS results. Our calculated  $O_{2p}$ - $Zn_{4s}$  separation of 1.5 eV lies within the uncertainty range of the UPS value, while the XPS value at 3.0 eV is twice as large. On the other hand, the  $\chi\alpha$   $Zn_{4s}$ - $Zn_{3d}$  separation is 2.3 eV, the XPS value is  $2.9 \pm 0.2$  eV, and the UPS value of  $4.7 \pm 0.4$  eV is almost twice as large. The calculated  $Zn_{3d}$ - $O_{2s}$  separation is 11.0 eV, and the XPS result gives  $11.9 \pm 0.2$  eV (no UPS results available). Comparison of the total energy spread from the VBM to the  $O_{2s}$  levels for the  $\chi\alpha$  model (15.2 eV) with the XPS results ( $20.7 \pm 0.1$ ) and consideration of the  $\chi\alpha$  small band widths discussed above lead to the conclusion that the  $\chi\alpha$  cluster model represents a "compressed" version of the experimental picture.

In the above discussion we did not consider the broadening effects of the spectrometer on the observed spectra. We will do so in the cross section results we present next.

Table 5.1. Comparison of experimental and calculated values for orbital features. All values in eV with respect to the VBM.

	PRESENT STUDY	UPS (REF. 4)	XPS (REF. 5)	OTHER <sup>a</sup>
O2p location <sup>b</sup>	-2.01	$-1.6 \pm 0.2$	$-2.9 \pm 0.1$	—
Zn4s location	-3.5	$-2.8 \pm 0.2$	$-5.9 \pm 0.1$	—
valence band width	2.3	$\sim 5$	$\sim 7$	$5-6^8$
Zn3d location	-5.8	$-7.5 \pm 0.2$	$-8.2 \pm 0.1$	$7.8^7, 8.5^6$
Zn3d width	.08	—	$\sim 2$	$2^7$
O2s location	-16.8	—	$-20.7 \pm 0.1$	$\sim 20^8$
O2s width	.2	—	$\sim 3$	$\sim 4^8$

<sup>a</sup>Superscript refers to the reference at the end of Chapter Five.

<sup>b</sup>The energy value at the center of the energy spread (for a given set of levels representing the particular state) is the value used for the location of that state.

### 5.3. Generation of $\chi\alpha$ Photoemission Spectra

Calculations using the SCF- $\chi\alpha$ -SW method result in cross section values for the individual molecular orbitals. This value represents the height of a delta function centered on the given molecular orbital. Experimentally however, the distributions of photoemitted electrons from the orbitals are not detected as delta functions but are instead spread out into bands.

Assuming conservation of electrons, the calculated cross section value (the ratio of the number of electrons/photon/area) must be proportional to the area under an appropriate electron energy distribution curve. Since we are concerned here only with relative intensity comparisons, we have set the calculated cross section value equal to the area under the curve. (Also see Section 5.6) The sum of the contributions from all the broadening effects (see Section 4.1) to this distribution curve can only be estimated. We have chosen a Gaussian distribution with a FWHM of .32 eV (which corresponds to the typically used value of  $\sigma = .01$  Rydberg to represent the true energy distribution from each molecular orbital. The sum of all these Gaussians then represents the true line intensity  $I(E)$  that is input to the detector. This

ORIGINAL PAGE IS  
OF POOR QUALITY

true curve  $I(E)$  is related to the recorded spectra  $O(E')$  by

$$O(E') = \int R(E - E') I(E) dE \quad (\text{Eq. 4.1})$$

where  $R(E - E')$  is the instrumental response function.

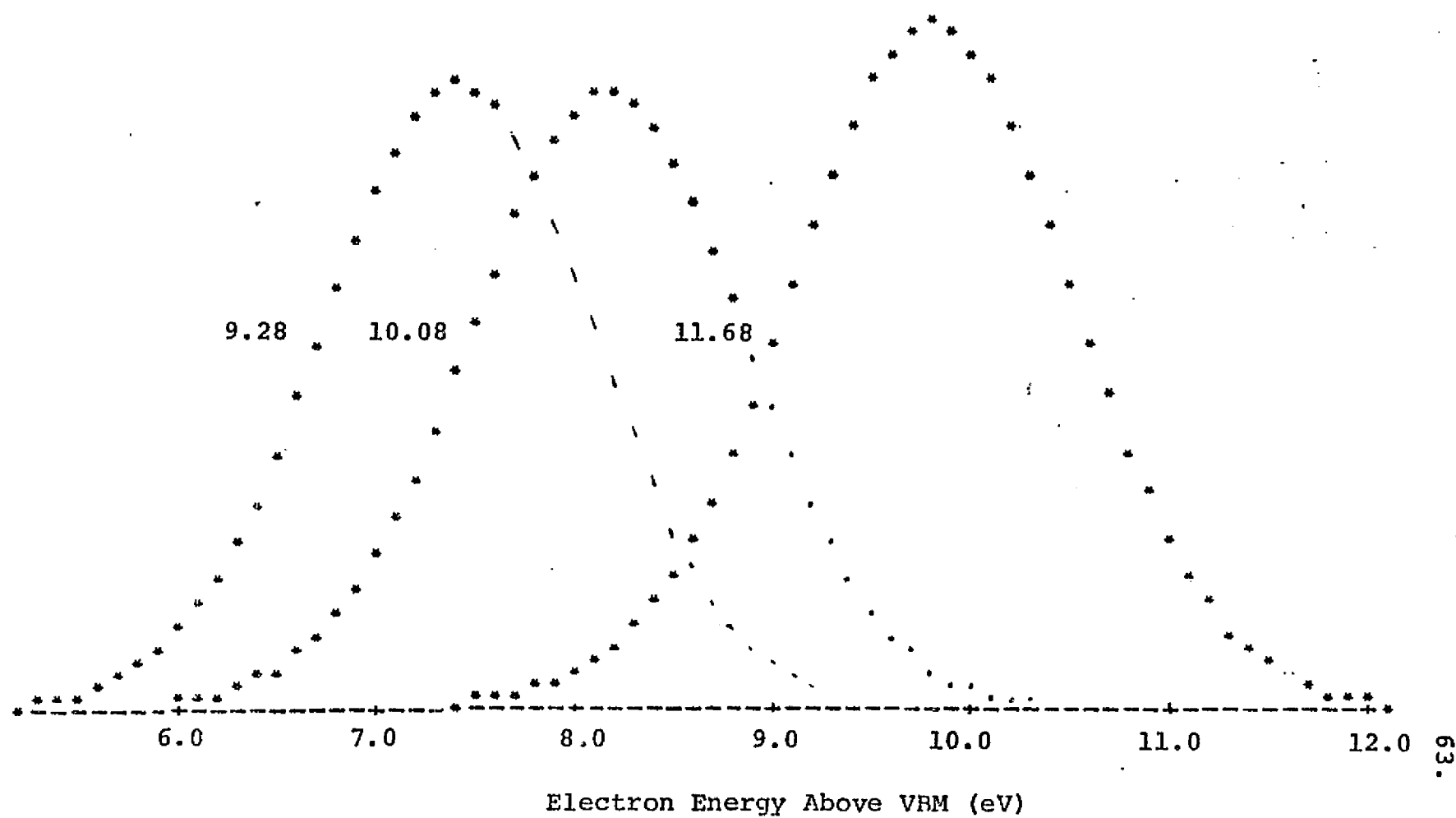
We have used Eq. 4.1 to computer generate  $\chi\alpha$  photoemission spectra which we present in Sections 5.4 and 5.5 for comparison to the experimental curves. The FWHM values used for the instrumental response function were those reported in the literature. For the XPS results we have used a Gaussian instrumental response function with a height of one and a constant FWHM value of .55 eV. For the UPS results we have also used a Gaussian instrumental response function of height one but with a FWHM value which is directly proportional to the kinetic energy of the electrons. The FWHM value used was 0.2 eV for a kinetic energy of 7.5 eV above the VBM.

#### 5.4. UV Photoemission Cross Sections

##### 5.4.1. Upper Valence Band

In Figure 5.3 we present our UV cross section results. We have plotted them as intensity versus kinetic energy for easy comparison to the experimental data, which is

Figure 5.3.  $\chi\alpha$  generated EDC's for  $\text{ZnO}_4^{-6}$  cluster; intensity is in arbitrary units.



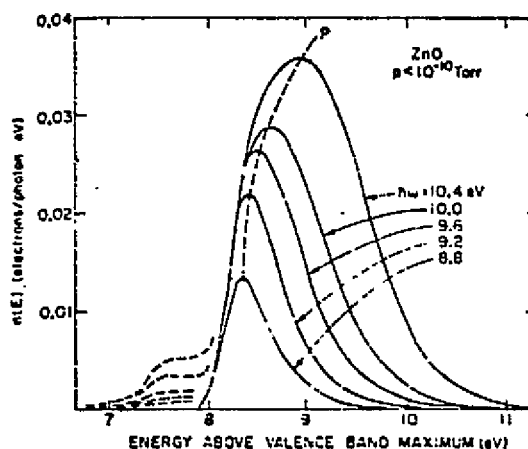
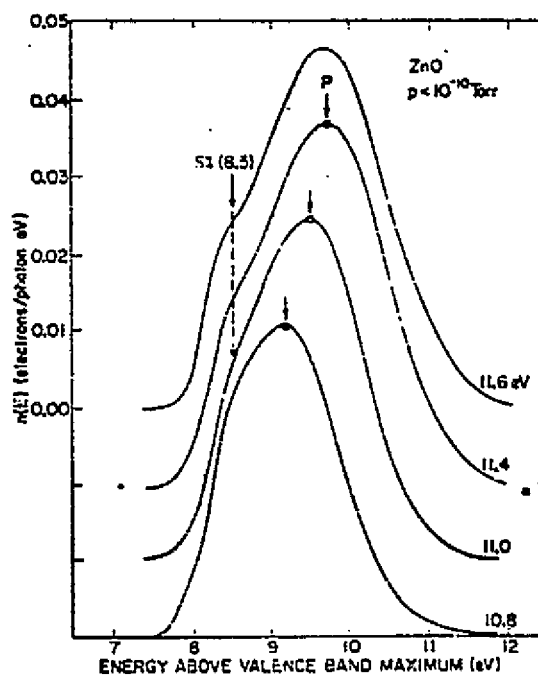


Figure 5.4(a). Normalized energy distributions of the photoemitted electrons.  $8.8 < h\nu < 10.4$  eV. The dashed curves represent contributions to the EDC's from the uncleaved-sample sides. Ref. 4.



ORIGINAL PAGE IS  
OF POOR QUALITY

Figure 5.4(b). Normalized energy distributions of the photoemitted electrons.  $10.8 < h\nu < 11.6$  eV. SI is attributed to conduction band structure. Ref. 4.



shown in Figures 5.4(a) and 5.4(b). The most outstanding features of the experimental curves are the overall growth with increasing incident photon energy. Notice also that not only has the intensity of the EDC's increased with increasing photon energy but also the energy range of emitted electrons has increased from  $\sim 1.7$  eV ( $h\nu = 8.8$  eV) to  $\sim 4.5$  eV ( $h\nu = 11.6$  eV), and more importantly the FWHM value has increased. In simple terms,  $E_k = h\nu - E_D$  (Eq. 1.1) so that if  $h\nu$  is increased by 0.4 eV, the  $E_k$  is also increased by that same amount. However, from the experimental EDC's one can see that for a photon increment of 0.4 eV, the peak is seen to shift approximately 0.2 eV.

All of these observations lead to the conclusion that the increase in intensity and energy distribution of electrons and the observed shift seen in the EDC's are due to contributions from the increasing number of accessible states as the photon energy probes deeper into the valence band. By  $h\nu=11.68$  all valence band states have been reached and the peak has stopped growing. This conclusion is further supported by our calculations. In Figures 5.5(a)-(e) we present the calculated cross section values as a function of photon energy for the individual molecular orbitals which comprise

Figure 5.5(a).  $\chi\alpha$  calculated cross section as a function of energy for molecular orbital  $7t_2$ .

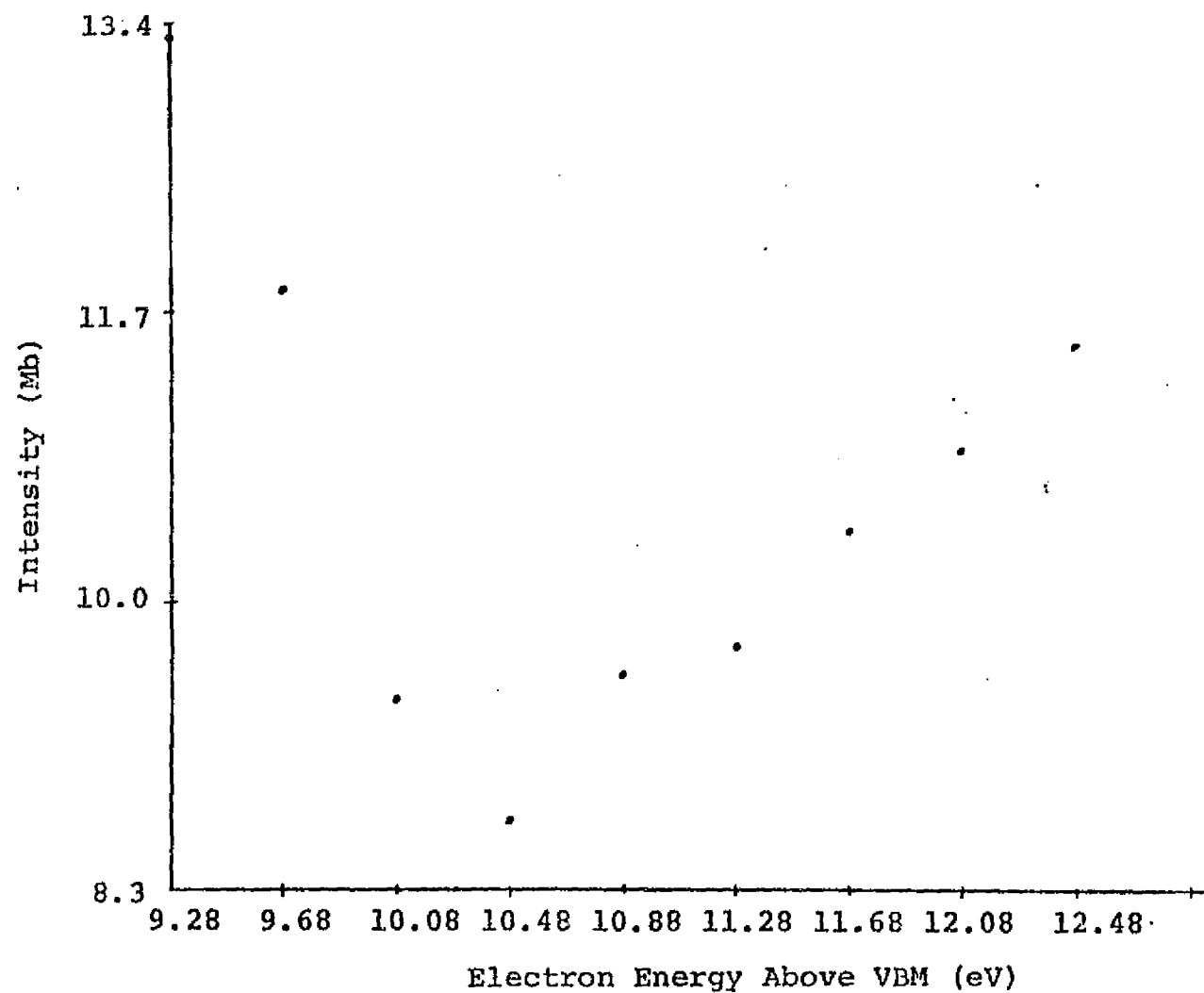


Figure 5.5(b).  $\chi\alpha$  calculated cross section for molecular orbital  $1t_1$ .

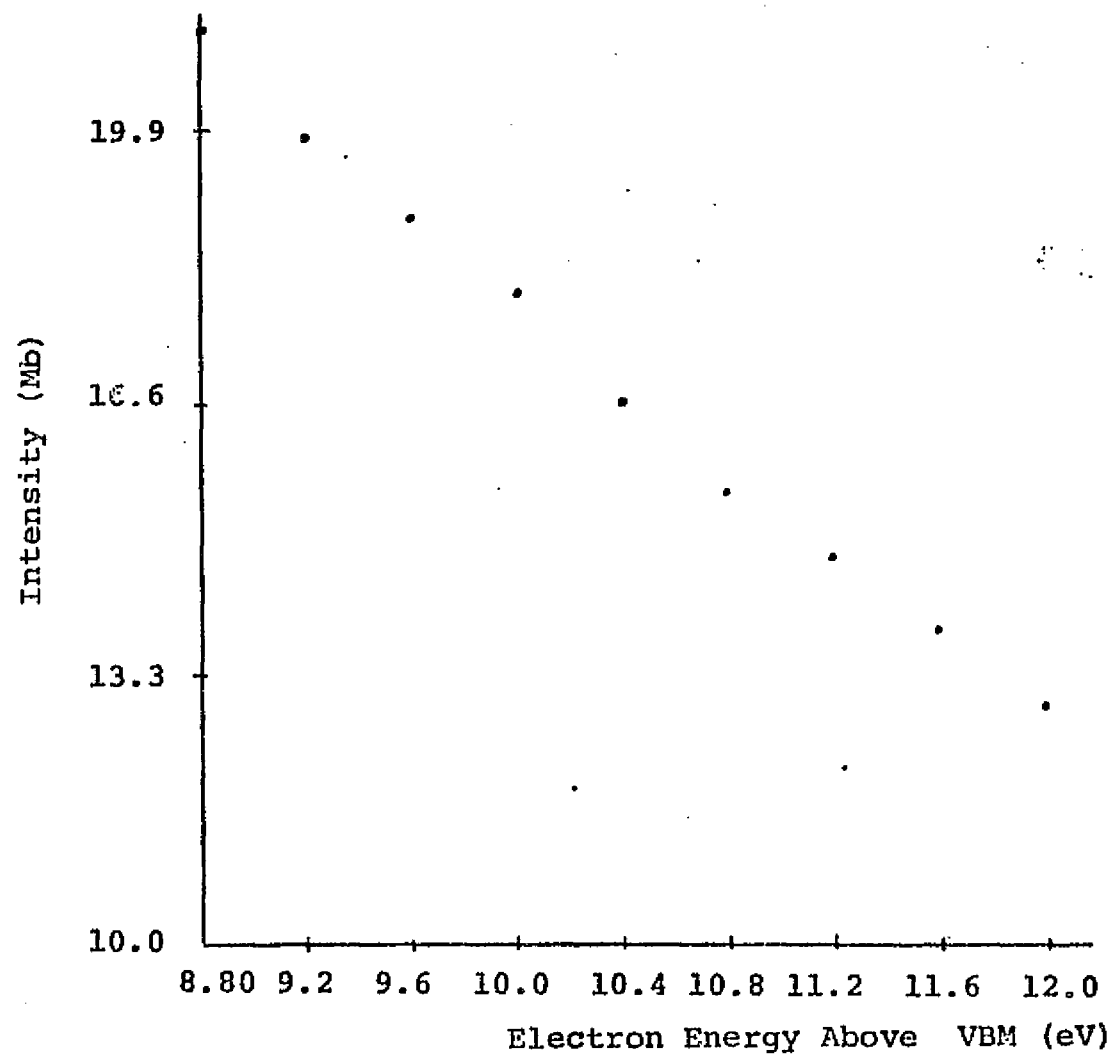


Figure 5.5(c).  $\chi\alpha$  calculated cross section for the 2e orbital.

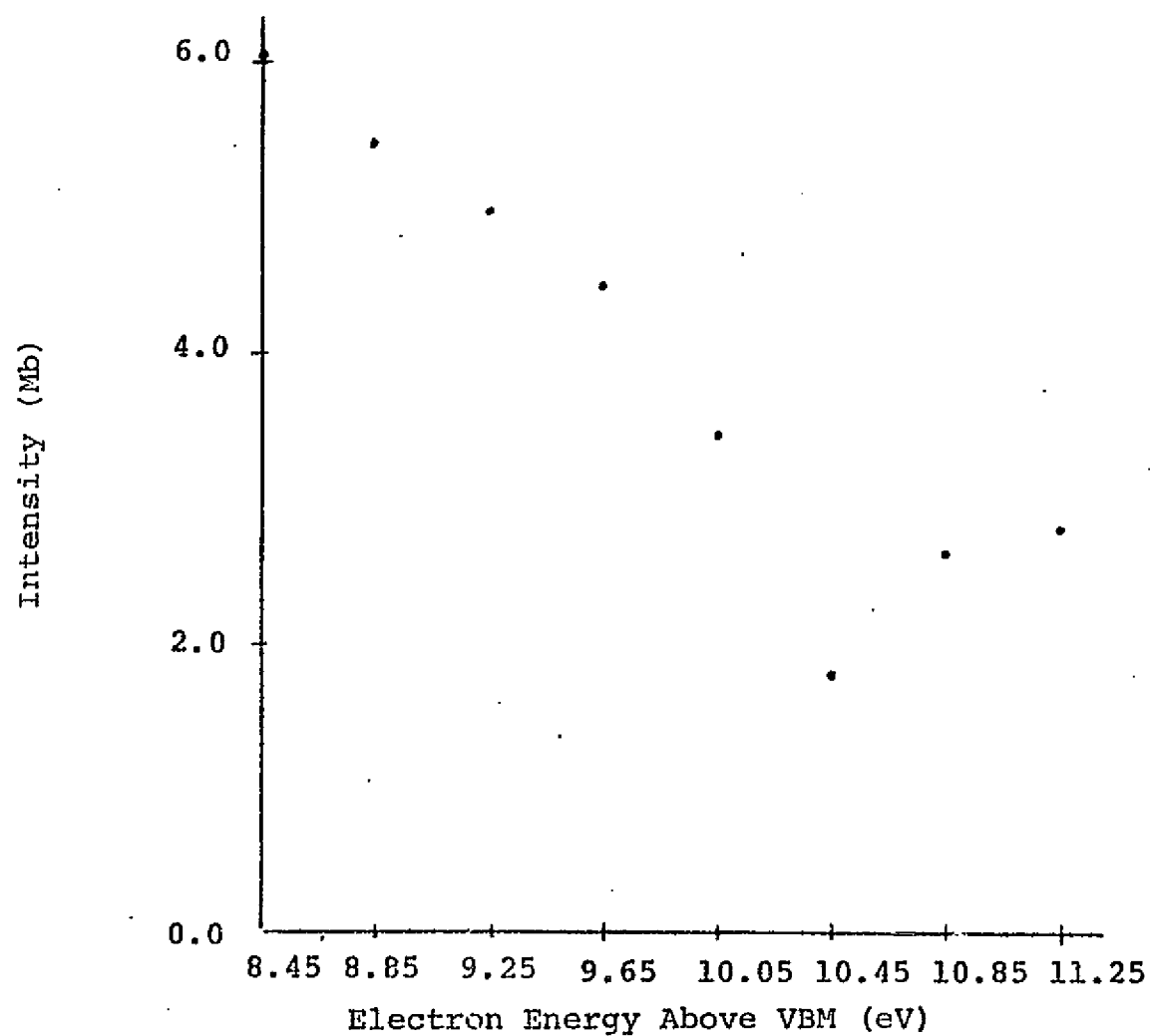


Figure 5.5(d).  $\chi\alpha$  calculated cross section for the  $6t_2$  orbital.

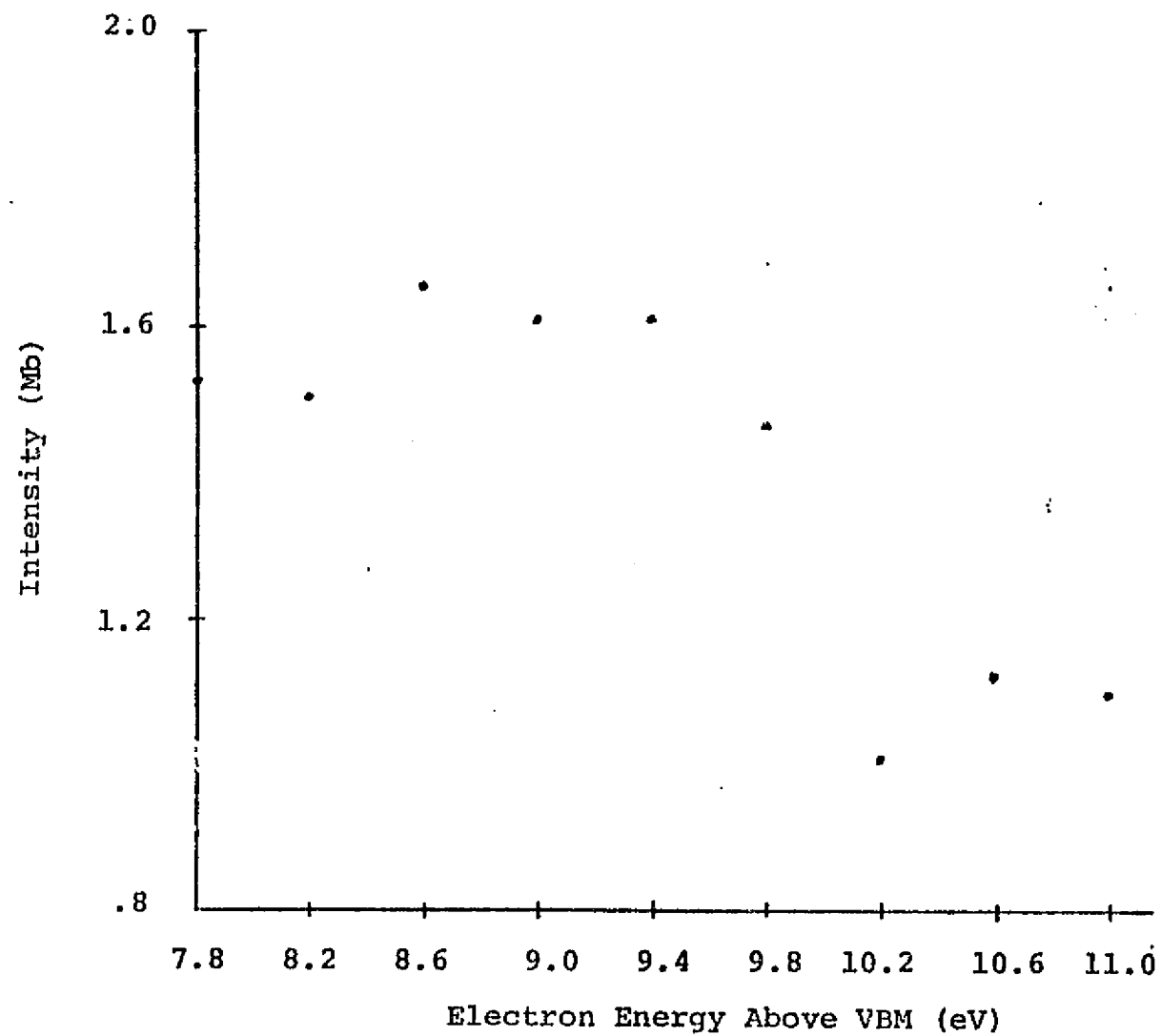
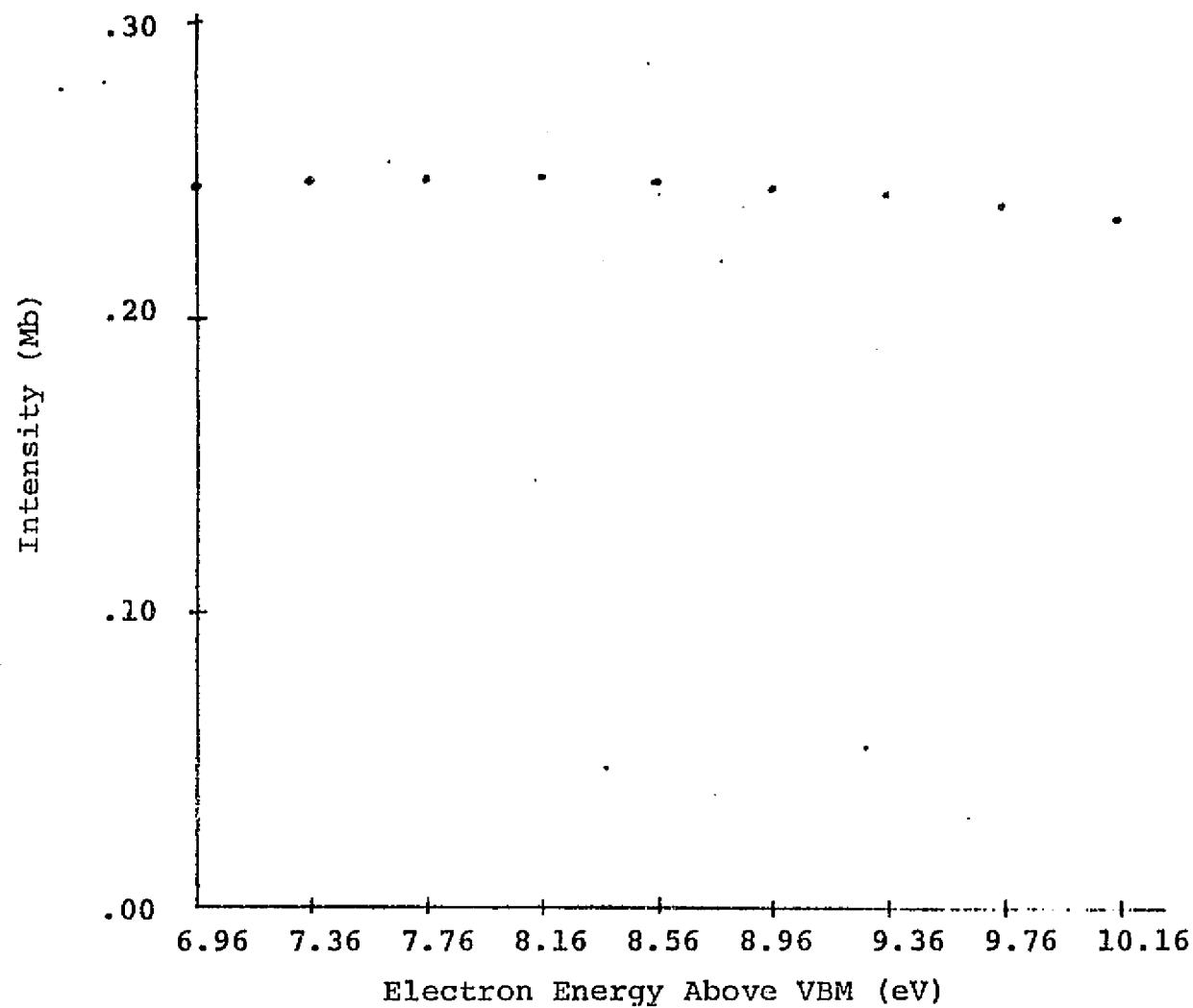


Figure 5.5(e).  $\chi\alpha$  calculated cross section for the  $2a_1$  orbital.



the upper valence band. From Figures 5.5(a) - (e) it can be seen that all of the individual cross section values actually show a decreasing trend with increasing energy; thus an increase in the number of accessible states is the most logical reason for the observed growth.

Our calculated EDC's presented in Figure 5.3 display the main trends of the experimental curves. Notice however, that the  $\chi\alpha$  EDC's do not grow as rapidly with increasing photon energy. Closer examination of the role of the valence band with in determining the EDC reveals that even for our lowest photon energy calculation ( $\hbar\omega = 9.28$  eV) our entire valence band contributes to the curve. Thus as we increase the photon energy in our calculations, the same five states, and only these five states contribute to the EDC. (Notice our FWHM is constant at 1.6 eV for all these curves.) In fact, from the decreasing trends in the cross sections in Figures 5.5(a) - (e) one would expect the intensity of the  $\chi\alpha$  EDC's in Figure 5.3 to decrease with increasing photon energy. This is not seen because we have included the effects of the ac retarding spectrometer. Since with this spectrometer the FWHM of the detector window increases with increasing electron energy, the high energy side of the curve is recorded larger than it really is. The magnitude of

the broadening effect can be seen in Figure 5.3. The low energy curve (9.28 eV) has an energy range of  $\sim 4.4$  eV, while the high energy curve (11.68 eV) has a range of 4.7 eV. Without the spectrometer broadening these energy ranges would be equivalent in our calculations.

Our calculated peaks shift by an amount equivalent to the photon energy shift whereas in the experimental curves (Figures 5.4(a) and 5.4(b)) the peaks are seen to shift more slowly than the corresponding photon energy increase. The additional valence states accessible to the higher photon energies lie deeper in energy and thereby contribute electrons on the low end of the energy scale. This results in a peak which shifts more slowly to the right than the corresponding photon change.

One other small point to mention is that our Gaussian broadening ignores the electron affinity of the ZnO surface, so that electrons can be predicted to leave the sample with kinetic energies less than the experimental threshold energy 7.8 eV. This can be seen in the 9.28 eV photon curve of Figure 5.3, where the electrons are predicted to escape with energies of 6.8 eV above the VBM. This effect was not more pronounced because our valence band width was small.



Comparison of the  $\chi\alpha$  curves with the experimental EDC's shows our 11.68 eV curve to be in excellent agreement with the data, while the 10.08 eV peak is at least 0.2 eV too low, and the 9.28 peak is at least 0.8 eV too low. This is completely reasonable since our 10.08 and 9.28 curves incorrectly contain contributions from all the valence levels, due to the inability of the ground state calculation to correctly predict the ZnO orbital spacings especially from such a small cluster. Imagine the 9.28 and 10.08 curves without the Gaussian contributions from the deeper lying valence states, i.e., with some of the left side of their curves cut away. This would cause the peaks to shift to the right (higher energies), in closer agreement with the experimental data. From this we conclude that the 11.68 eV curve is a good representation of the ZnO valence band structure. It may be noted though the FWHM is 1.6 eV in the  $\chi\alpha$  curve, as opposed to 2.3 eV in the experimental EDC. This again is due to the incorrect spacing of the molecular orbitals.

#### 5.4.2. Zn3d Band

The UPS study reports the location of the Zn3d band at 7.5 eV below the VBM. Thus the d bands were not accessible to the photon energies discussed in Section

Figure 5.5(f).  $\chi\alpha$  calculated cross section for molecular orbital 1e.

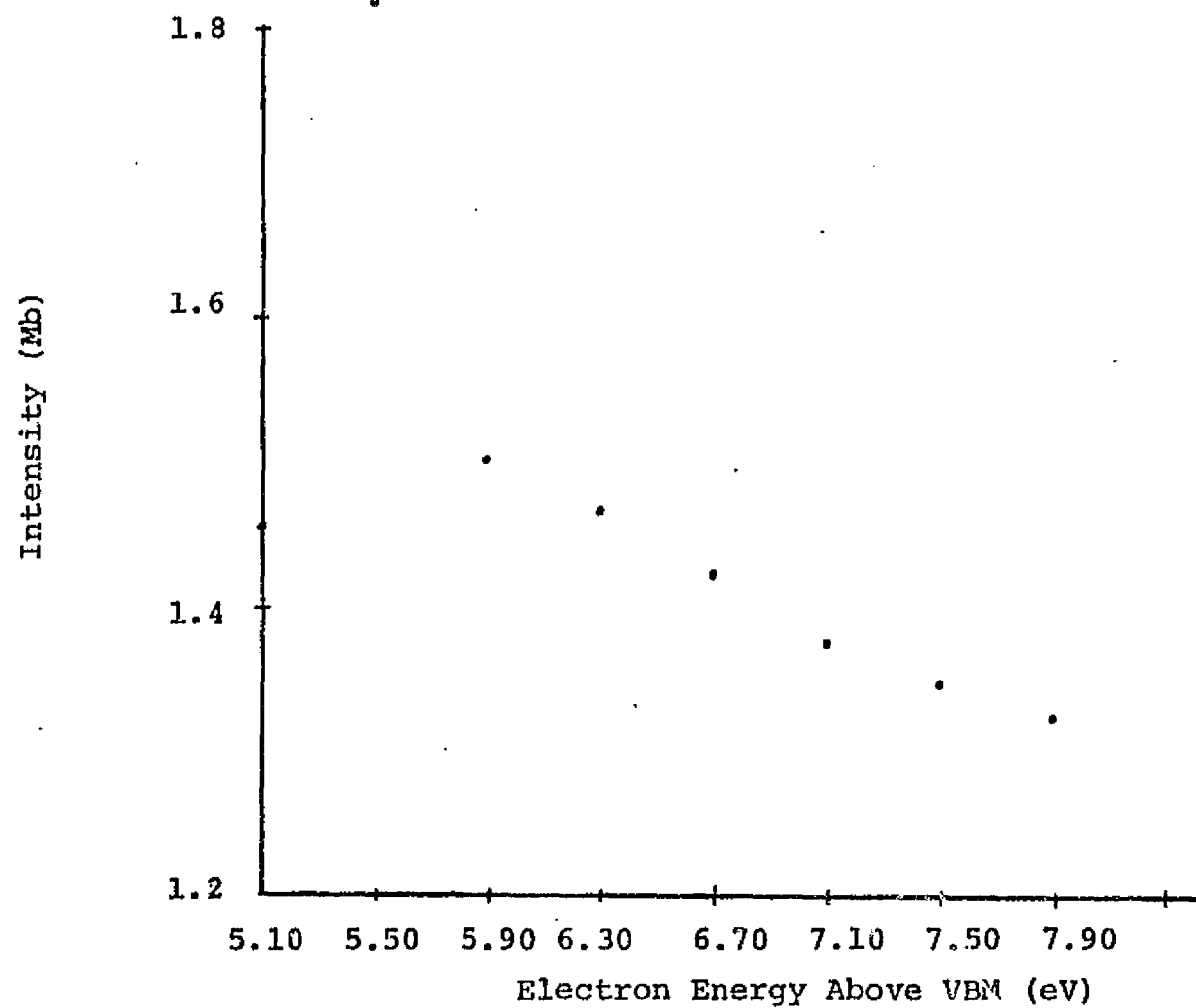
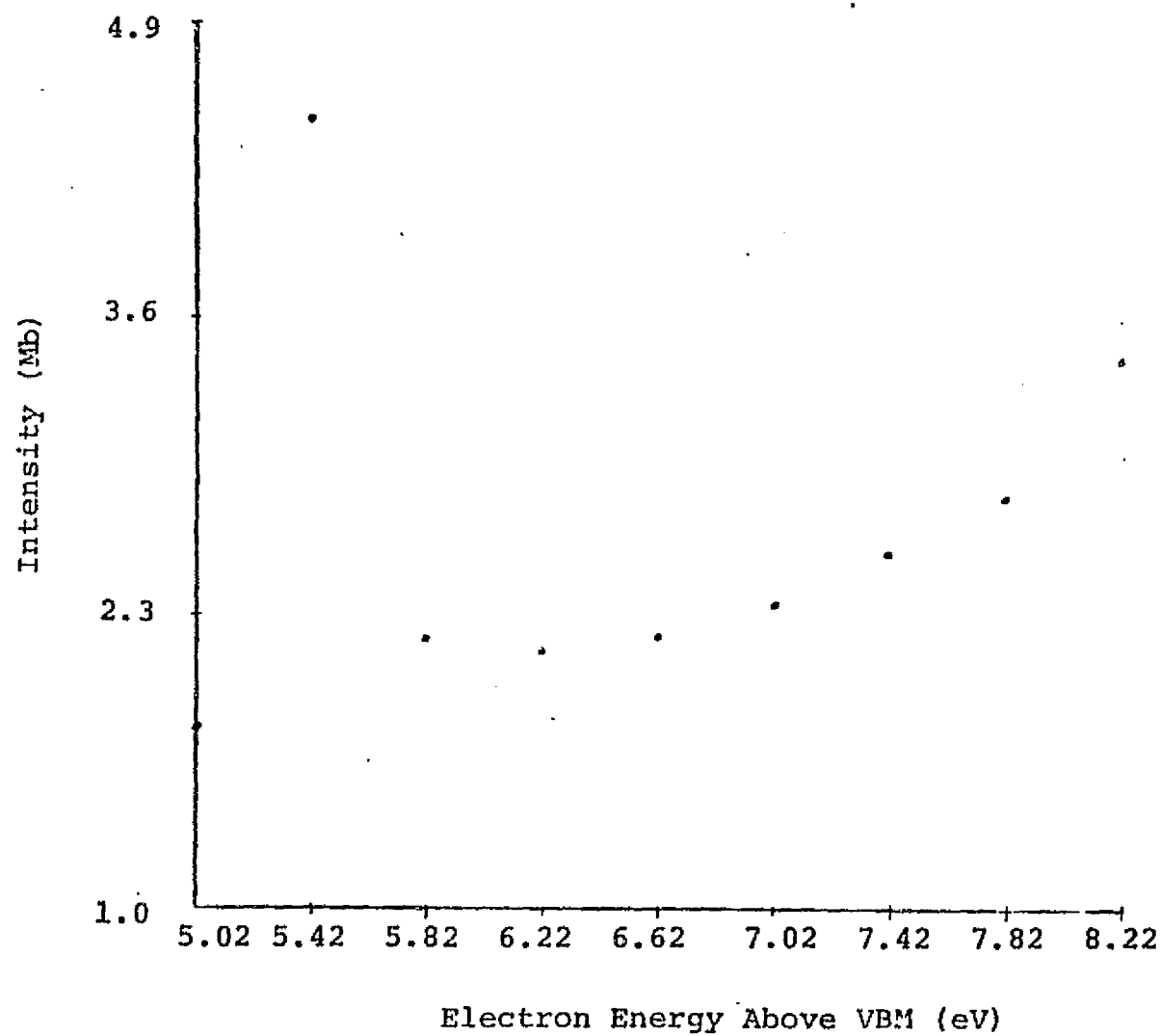


Figure 5.5(g).  $\chi\alpha$  calculated cross section for the  $5t_2$  orbital.

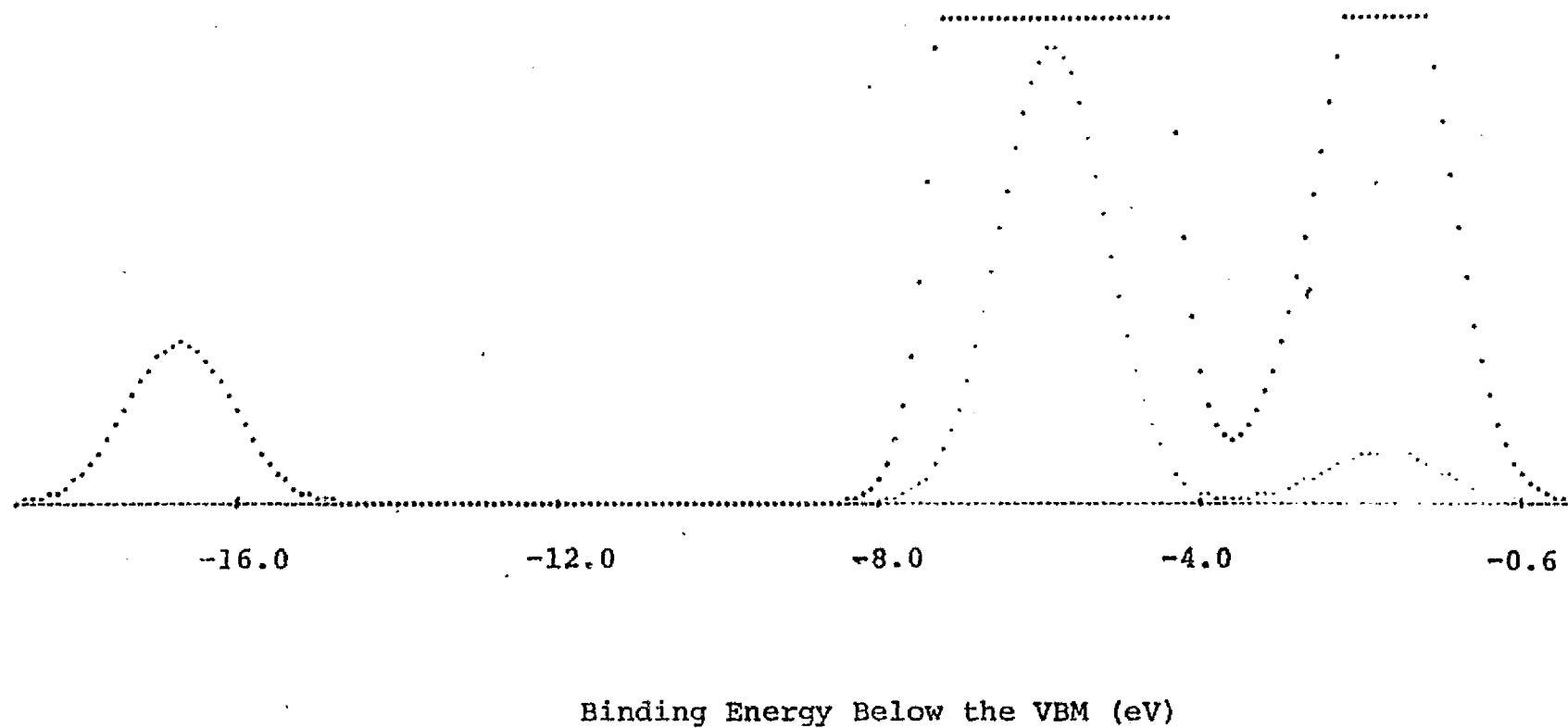


5.4.1. However, the  $\chi\alpha$  ground state calculation predicted the location of the Zn3d level to be at -5.8 below the VBM so that our 3d band was accessible to even the 9.28 eV photons. (Recall that the transition state calculations (Section 4.4) of the  $\chi\alpha$  method were able to predict the location of the 3d levels much more accurately.) The cross section values calculated for both of the Zn3d-like states ( $1e$ ,  $5t_2$ ) are presented in Figures 5.5(f)-(g). Note that the intensities are typical of those of the valence band, as expected. While the UPS study did measure photoemission from the 3d bands, a direct comparison to our results is not possible since the photon energy and hence the electron energy was much higher than ours.

### 5.5. X-ray Photoemission Cross Sections

In Figure 5.6 we present our X-ray cross section results. The corresponding experimental results are shown in Figures 5.7(a) and 5.7(b). Figure 5.7(a) is the "raw" X-ray spectra. Here the most prominent feature is the intense Zn3d spike centered about 12 eV below the Fermi level. At binding energies from 4 eV to 9 eV below the Fermi level lie two valence band peaks, and some 10 eV and 17 eV below the Zn3d level lie two more peaks. Much of this deeper lying structure has been attributed to a

Figure 5.6.  $\chi\alpha$  generated X-ray spectra for the  $\text{ZnO}_4^{-6}$  cluster. Intensity is in arbitrary units. The valence band and 3d peaks are also shown reduced by a factor of 12.



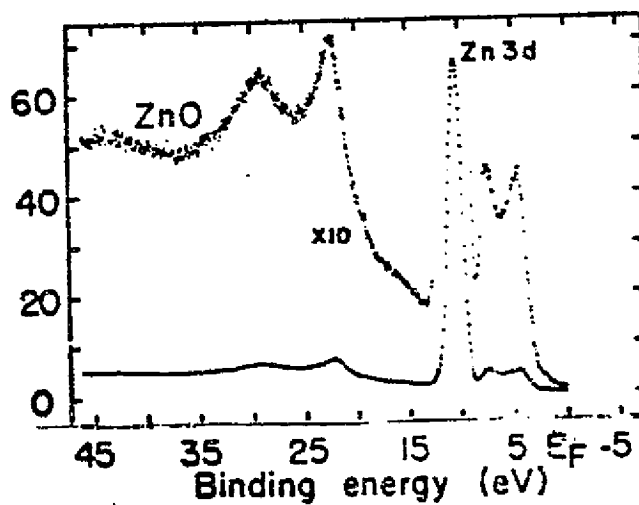


Figure 5.7(e). X-ray photoelectron spectra ZnO. Ref. 5.

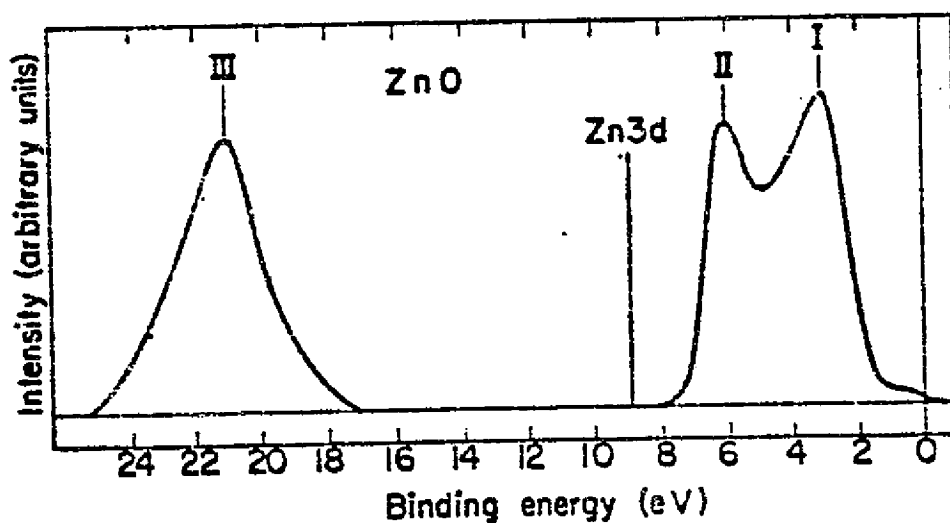


Figure 5.7(b). Corrected valence-band spectrum I'(e) of ZnO. Binding energies are given with respect to the VBM. Ref. 5.

plasmon excitation.<sup>9</sup> The  $\chi\alpha$  spectrum shown in Figure 5.6 appears to reproduce the basic features of the XPS results. Comparison of the area under the 3d spike and that under the total upper valence band structure in Figure 5.7(a) shows the 3d peak to be roughly six times larger. The corresponding measurement on our generated X-ray curve resulted in a 3d/valence band ratio of 7.8. Figure 5.7(b) shows the corrected experimental spectra. The 3d level lies at  $-8.8 \pm 0.1$  eV, the O2p peak at  $-2.9 \pm 0.1$  eV, the Zn4s at  $-5.9 \pm 0.1$  eV, and the O2s peak at  $-20.7 \pm 0.1$  eV, all with respect to the VBM.

In the corrected spectra the Zn3d band has been subtracted along with the contribution from inelastically scattered electrons (including those attributed to the plasmon excitation). The ratio of the area under the O2s peak (labelled III in Figure 5.7(b)) to the valence band structure (labelled I and II) is approximately 1.5, while the corresponding ratio from our calculations is 4.4. Since the theoretical and experimental ratios of the Zn3d peak area to the area of the valence band structure are in reasonable agreement, we conclude that the  $\chi\alpha$  model predicts the O2s feature to be roughly three times smaller than that attributed to it in Figure 5.7(b).

Comparison of the overall XPS picture with our generated

spectra again shows our MO levels to be spaced too closely. Because of the compressed valence band in the  $\chi\alpha$  model, only one valence band peak is resolved in our generated spectra. Also the peak separation between the calculated 3d band and the  $O_{2s}$  band is 10.9 eV, while the experimental values is 11.9 eV.

Notice that the energy scale in the theoretical spectra does not coincide with that of the X-ray spectra. Our  $\chi\alpha$  spectra was generated by placing the highest occupied orbital,  $7t_2$ , -1.6 eV below the VBM, i.e., a Gaussian distribution of electrons assumed for that state was centered at -1.6 eV, the location of the  $7t_2$  level predicted from the UPS results. Our X-ray calculations show that our one valence band peak is due mainly to the  $7t_2$  level, so that it corresponds to the first peak in the XPS curve, which the experimentalists place -2.9 eV below the VBM. Thus there is a discrepancy of about 1.3 eV in the location of the VBM between the UPS and XPS data.

In order to compare our results with those of XPS, we need to shift our spectra about 1.3 eV to the left (deeper energy) to line up the first peaks of both spectra. Then our resultant peaks lie at -7.1 (3d), -2.9 eV (valence band), and -18.0 eV ( $O_{2s}$ ) with respect to the XPS VBM.

One other interesting point to mention is that while



our valence band consists of five states, our X-ray calculations predict the entire valence band structure is due mainly to states  $7t_2$  and  $2e$ , with a contribution ratio of approximately 3/1. If we equate the  $7t_2$  level with the peak I in Figure 5.7(b) and the  $2e$  level with peak II, then XPS predicts an orbital separation of 3.0 eV. We will come back to this idea in Section 5.7.

In Chapter 2 it was pointed out that the  $\chi\alpha$  method uses the dipole approximation, which is valid when the incident wavelengths are large compared to atomic dimensions. Mathematically, the dipole approximation consists of expanding the function  $e^{-ikr}$  in a power series and then dropping all terms but the first. Since  $e^{-ikr}$  can be expanded as

$$e^{-ikr} = 1 - ikr - \frac{(kr)^2}{2} + i \frac{(kr)^3}{6} + \frac{(kr)^4}{24} - i \frac{(kr)^5}{120} + \dots$$

this approximation is valid if  $kr < 1$ . For the X-ray energy of 1486.6 eV,  $k \approx .75\text{\AA}^{-1}$ , so that at our outer-sphere boundary ( $r_{\text{out}} = 2.70\text{\AA}$ ) the approximation is not valid. However, within the atomic spheres ( $r_{\text{zinc}} = 1.1\text{\AA}$ ,  $r_{\text{oxy}} = .8\text{\AA}$ ) it is valid. For each initial state, at least 83% of the charge density was contained within the outersphere, and the majority of it in the atomic spheres, with the exception of the  $6a_1$  and  $6t_2$  levels, which contained

only 5% in the atomic regions, and 94% and 80% in the intersphere regions, respectively.

#### 5.5.1. Modulating Effects

It was pointed out earlier (Section 5.2.1.) that XPS and UPS measure somewhat different quantities. The basis for this argument stems from the modulating effects important at different energies. At UV energies, both the initial and final state density modulation is important, along with the actual cross section modulation. At XPS energies, final state densities are fairly constant since the transition energy far exceeds the variations in the crystal potential energy of the valence electrons.<sup>10</sup>

Cross section modulation can be understood in terms of the sensitivity of photons of differing energy<sup>11</sup>, UV photons are more sensitive to the outer portion of the wavefunction, i.e., far from the nucleus, while XPS senses the wavefunction near the nucleus. This effect can be seen from the form of the photoemission matrix element:

$|\langle f | \vec{r} | i \rangle|^2$ . Whenever the curvature of the initial state radial wavefunction matches that corresponding to the final state wavefunction, the cross section value will be highest. An example of this effect is shown in Figure 5.8. for the

2s and 2p radial wavefunctions of carbon.

#### 5.6. UV Intensity Comparison

Up to this point we have been concerned with comparing the experimental and theoretical cross section peaks on a relative basis. In this section we present the  $\chi\alpha$  "absolute" cross section intensities in the UV range for which experimental results are available. (See Appendix B.)

The problem we are concerned with here is to compare the theoretical cross section values for a cluster of five atoms to the experimental results for the microscopic solid. The  $\chi\alpha$  photoemission computer program calculates the cross section from the probability of an absorbed photon to cause an electron to be emitted from a particular orbital. The contributions from all the orbitals then gives the total cross section for the cluster. The cross section values are given in units of area, the area representing the effective size of the orbital to that particular photon energy.

The experimentalists report their results for a particular photon energy in units of the ratio of the number of emitted electrons to the number of photons, a dimensionless quantity. Thus in order to compare results, we must convert our results to the ratio of the number of

electrons to the number of photons. This we did on a relative basis in order to generate the  $\chi\alpha$  spectra in Sections 5.4 and 5.5 (See Section 5.3). But now to get a normalized spectrum we must construct a solid out of our microscopic cluster. We can assume that this solid consists of some multiple of clusters, the number depending upon the effective size of the experimental sample, which in turn depends upon the photon attenuation and the electron escape depth.

The electron escape depth is the limiting factor here, but unfortunately no values for ZnO have been reported in the literature. However, Lindau and Spicer<sup>12</sup> have published a plot of electron escape depths (Figure 5.9) for several different materials. From Figure 5.9 it appears that most material seem to lie on or near a "universal" curve. If we assume that ZnO also lies on or near the curve, the expected escape depths would be somewhere in the range of 1-40<sup>o</sup>Å for electrons of kinetic energies in the range of 7-12 eV above the VBM. Using the concepts of electron escape depth and photon attenuation depth, we have developed a solid model from clusters to represent the effective experimental sample.

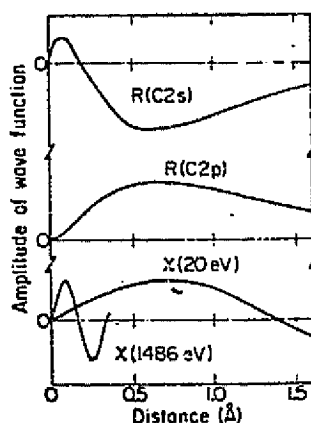
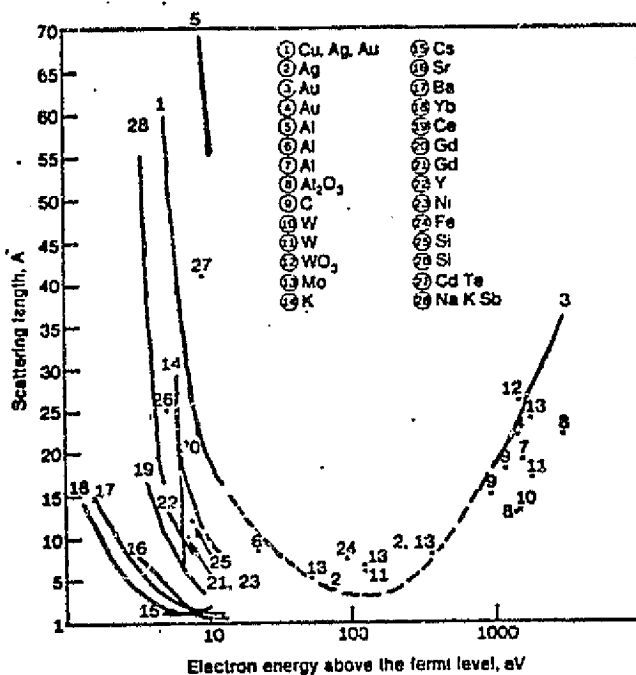


Figure 5.8. Amplitudes of the radial 2s and 2p wave functions of carbon,  $R(C\ 2s)$  and  $R(C\ 2p)$  compared with the radial wave functions of free electrons,  $\chi$ , in states corresponding to 20- and 1486-eV kinetic energy, respectively Ref. 5.



ORIGINAL PAGE IS  
OF POOR QUALITY

Figure 5.9. Electron scattering lengths for electrons traversing the given material. Energies are with respect to the VBM for nonmetals and with respect to the Fermi energy for metals. Ref. 12.

### 5.6.1. Solid Model from Clusters

Let us define a scattering center equal to one  $\text{ZNO}_4^{-6}$  cluster. The spacing between scattering centers is  $2.29\text{\AA}$ , leading to a number density  $n$  of .0825 centers/ $\text{\AA}^3$ . Assuming an exponential attenuation of photons, then the total number of electrons emitted from an elemental thickness  $dz$  at depth  $z$  is

$$N_e(z)dz = I(z)n\sigma dz \quad (5.1)$$

where  $I(z) = I_0 e^{-n\sigma z}$  is the photon intensity at depth  $z$ ,  $\sigma$  is the cross section (calculated by the  $\chi\alpha$  method) and  $\tau$  is the escape depth of the electrons. The total number of electrons at depth  $z$  times the average probability of electron escape gives the number of electrons escaping from elemental thickness  $dz$  at depth  $z$ . Thus, to get the total number of electrons escaping from the solid, we must then integrate over  $z$ :

$$N_{\text{tot}} = \int dz N_e(z) \int d\Lambda(\theta, \phi) f(\theta, z, \tau) / \int d\Lambda(\theta, \phi). \quad (5.2)$$

$$\text{The integral } \int d\Lambda f(\theta, z, \tau) / \int d\Lambda \quad (5.3)$$

is the average probability of escape, depending still upon  $\tau$  and  $z$ . The function  $f(\theta, z, \tau)$  is the probability of an electron escaping from the solid with angle  $\theta$ , escape

depth  $\tau$ , and from a depth of  $z$ . We choose to represent this function by the exponential

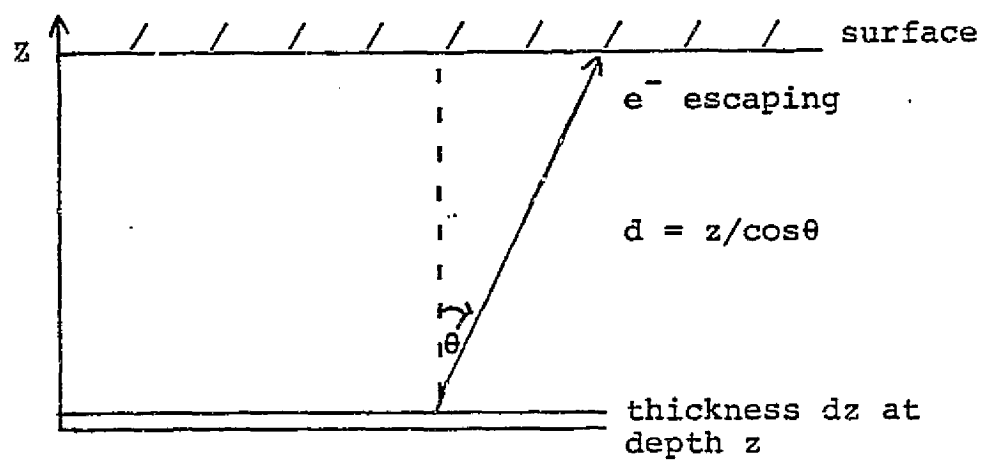
$$f(\theta, z, \tau) = e^{-z/\tau \cos \theta} \quad (5.4)$$

for  $0 \leq \theta \leq \pi/2$ , otherwise defined as zero.  $z/\cos \theta = d$  is the distance the electron must travel to escape (See Figure 5.10). It may be noted that  $f(\theta, z, \tau) = e^{-d/\tau}$  becomes  $1/e$  when  $\tau = d$ , i.e., when the electrons travel one escape depth their probability of escape has been reduced to  $1/e$ .

The next step is to set limits for the integrals in Eq. 5.2. The integral  $\int d\Lambda$  is over all angles and is just  $4\pi$ . The integral  $\int d\Lambda f(\theta, z, \tau)$  is over all angles, but note that while  $f(\theta, z, \tau)$  is defined as zero for  $\pi/2 < \theta < 2\pi$ , the angle  $\theta$  is taken over all  $2\pi$  angles, so that the integral may be taken equivalently over the upper hemisphere. Thus we are saying that those electrons emitted in the direction downward from the surface never escape. The integral over  $z$  may be taken from 0 to  $\infty$  for mathematical convenience, since the contributions from large  $z$  are negligible due to the exponential nature of the scattering depth  $\tau$ . Then Eq. 5.2 becomes

$$N_{\text{tot}} = I_0 n \sigma \int_0^\infty e^{-\sigma n z} dz \int_{\text{upper hemisphere}} e^{-z/\tau \cos \theta} d\Lambda / 4\pi \quad (5.5)$$

FIGURE 5.10. Diagram of electron escape from our solid model.





We solve this equation in Appendix A. The resulting equation is

$$\frac{N_{\text{tot}}}{I_0} = \frac{1}{2} \left\{ 1 - \frac{\ln(1+n\sigma\tau)}{n\sigma\tau} \right\} \quad (\text{A.4})$$

Notice that Eq. A.4 is approximately equal to

$$\frac{N_{\text{tot}}}{I_0} \approx \frac{1}{2} \left\{ 1 - \left( \frac{a - a^2/2}{a} \right) \right\} \approx 1/4 a \quad (\text{for small } a) \quad (5.6)$$

where  $a = n\sigma\tau$ . It is reassuring that  $N_{\text{tot}}/I_0$  is approximately linear in  $a$  since that is the assumption we made when we compared the relative sizes of our generated spectra to those of the experimentalists.

Notice also that we are making the approximation that  $\tau$  is constant, and we are completely neglecting electron-electron scattering, i.e., either the electron makes it out of the solid with all its energy or else it does not make it out at all. From the form of Eq. A.4 we realize that while  $\sigma$  and  $n$  are set values, we are free to choose a value of  $\tau$  such that we obtain the desired value of  $N_{\text{tot}}/I_0$ . The obvious restriction being that  $\tau$  is physically reasonable. Just as crucial in this curve fitting process is the chosen value of the FWHM to use for Gaussian broadenings of each of the individual  $N_{\text{tot}}/I_0$ 's (which correspond to the original  $\sigma$ 's) which sum to the true

integrated line intensity. We point out that a FWHM value of 0.1 eV and a  $\tau$  of  $15\text{\AA}$  resulted in an intensity five times too large, while a FWHM value of .32 eV and a  $\tau$  of  $8\text{\AA}$  gave intensities within 70%. Thus we see that this curve fitting process is somewhat arbitrary unless one of these parameters is known accurately.

### 5.6.2. Solid Model Cross Sections

Since only our 11.68 eV curve correctly represents cross section contributions from all the valence levels, we present our normalized 11.68 eV EDC in Figure 5.11. The figure was generated by calculating  $N_{\text{tot}}/I_0$  for each of the five contributing orbitals, assuming a Gaussian distribution function whose area equals the value of  $N_{\text{tot}}/I_0$  and a FWHM of .32 eV, and finally summing the Gaussians and multiplying by the detector response function and then integrating with respect to the energy. A direct comparison between the theoretical and experimental curves is shown in Figure 5.12. From the figures we see that our model predicts reasonable intensities with a FWHM value of .32 eV and a  $\tau$  of  $8\text{\AA}$ . However, we feel that while .32 eV is probably a reasonable broadening value, the true value for  $\tau$  may be slightly larger, so that our model predicts absolute intensities too large. This is

Figure 5.11. Normalized EDC employing the solid model  
from clusters for the  $\hbar\omega = 11.68$  eV curve.

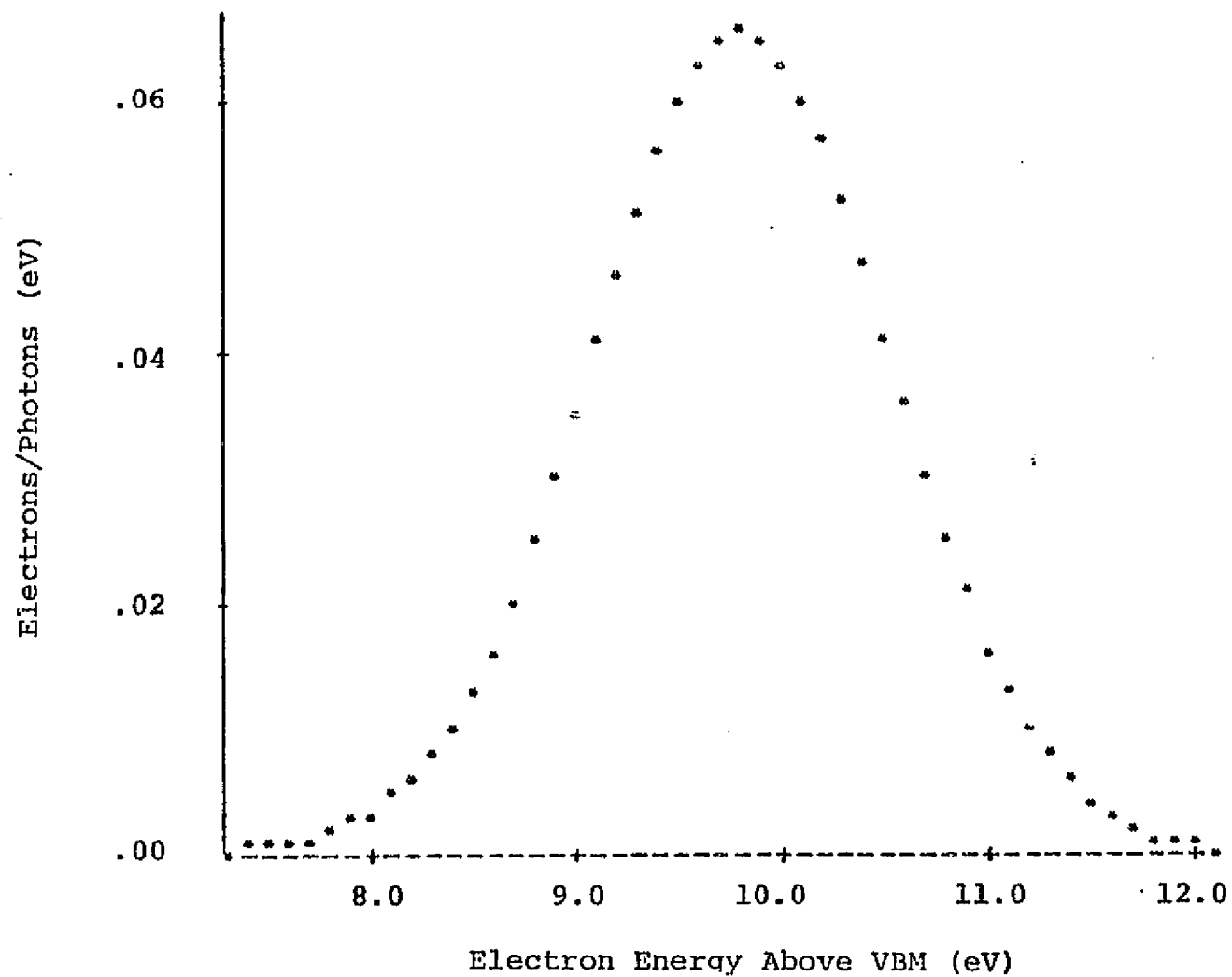
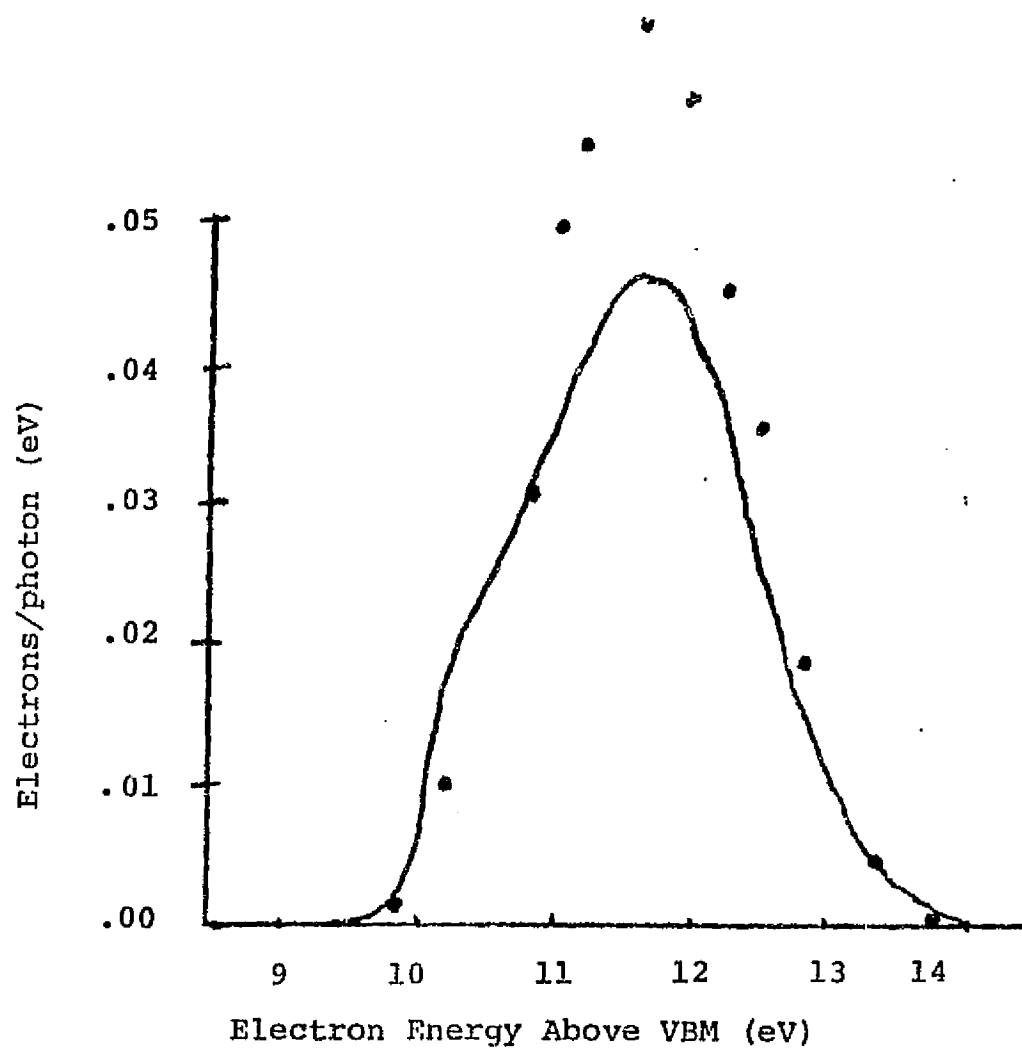


Figure 5.12. Direct comparison of theoretical 11.68 eV curve (dotted line) and the experimental EDC (solid line).



reasonable since our model does not account for those electrons inelastically scattered such that they have insufficient energy to escape the ZnO electron affinity, nor does it consider Auger or phonon processes.

### 5.7. Conclusion

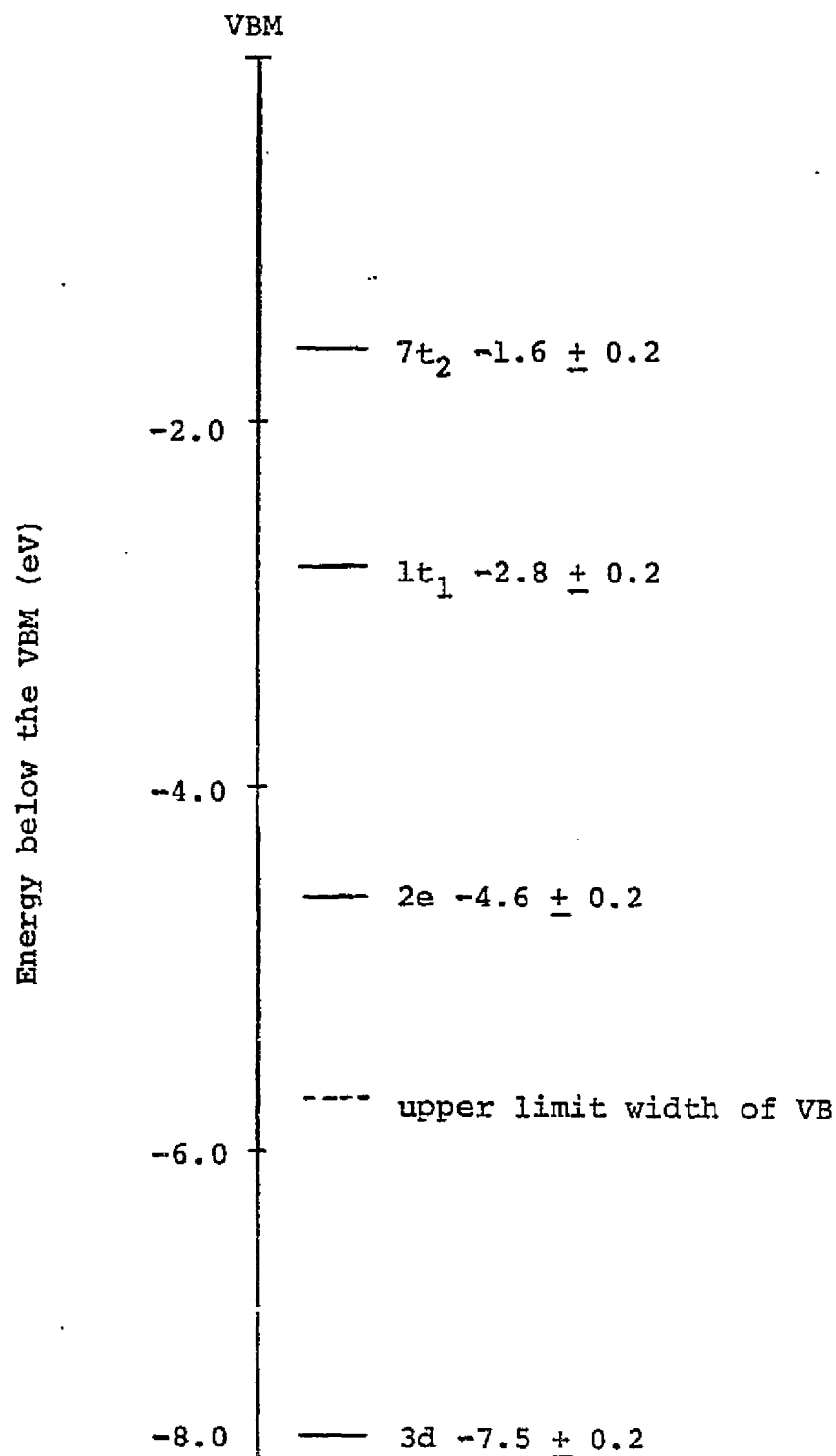
The basis for photoelectron spectroscopy serving as a tool in the determination of electronic structures lies in the fact that cross sections change as a function of energy, enabling identification of the molecular orbitals. Any theory capable of predicting these changes would certainly represent a reasonably accurate model of the molecular bonding.

The  $\chi\alpha$  generated spectra has shown the basic trends in both the UPS and XPS results; however due to the "compressed"  $\chi\alpha$  MO structure we could not resolve two peaks in our X-ray valence band structure, nor obtain the growing effect of increasing contributing states as seen in the UPS results.

Armed now with the relative intensities of the various molecular orbitals, we can construct a MO structure from the experimental results with the correct spacing. Let us assume our ordering in Figure 5.2 is correct. Since our cross section calculations show large

intensities for the  $7t_2$  level in both the UV and X-ray energies, we can use this first peak to "line up" the X-ray and UV spectra. We will use the UPS VBM since the structure seen at 0-2 eV in the XPS data (Figure 5.7(b)) probably represents photoemission from surface states. From Table 5.1 we see that the UPS results show a second peak at  $-2.8 \pm 0.2$  eV, and our UV calculations (Figures 5.5(a)-(e)) show that only one other state besides the  $7t_2$  has considerable intensity, that is the  $1t_1$  state. Thus we assign this location to the  $1t_1$  levels (See Figure 5.13). Looking back to the XPS results we see a second peak at  $3.0 \pm 0.2$  eV below their first peak. Our X-ray calculations tell us that only one other state besides the  $7t_2$  state has considerable intensity: the  $2e$  state. Thus we assign this experimental X-ray peak at  $4.6 \pm 0.2$  eV (below the UPS VBM) to the  $2e$  state. From the corrected X-ray spectra in Figure 5.7(b) we see that the valence band essentially ends  $1.1 \pm 0.1$  eV below the second peak, or according to our scale at  $5.7 \pm 0.2$  eV below the VBM. Thus this can be set as the upper limit on the width of the valence band. If however the valence band structure (left end of feature) seen in the XPS corrected spectra is due to say electron-electron scattering and the  $6t_2$  and  $6a_1$  states are actually very close to the

Figure 5.13. MO diagram for ZnO predicted from our calculated orbital intensities and the experimental data.



2e level, then the valence band width becomes  $4.6 \pm 0.3$  eV, which serves as the lower limit of the VB width. Finally, the UPS results place the Zn3d level at  $7.5 \pm 0.2$  eV below the VBM; the XPS results place it at  $8.8 \pm 0.1$  eV below their VBM which also corresponds to  $7.5 \pm 0.2$  eV below the UPS VBM. Thus with a knowledge of the cross section relative intensities one can deduce the orbital structure from the photoemission data. We show this cross section-determined MO diagram for ZnO in Figure 5.13.

#### 5.8. Summary

With a knowledge of the photoemission cross sections, X-ray and UV photoelectron spectroscopy are seen to complement each other in providing information on the orbital spacings of ZnO. Together with the  $\chi\alpha$  model of bonding, the cross section values allow a complete determination of the electronic structure of ZnO. However, more calculations need to be carried out to verify the "universality" of this method in determining electronic structures of other metallic compounds. Also more work needs to be done to establish a criterion for choosing a cluster size.



CHAPTER FIVE REFERENCES

1. W.N. Unertl and J.M. Blakely, Surf. Sci. 69, 23 (1977).
2. K. Schwarz, Phys. Rev. B 5, 2466 (1972).
3. R.P. Messmer, S.K. Knudson, K.H. Johnson, J.B. Diamond, and C.Y. Yang, Phys. Rev. B 13, 1396 (1976).
4. R.A. Powell, W.E. Spicer, and J.C. McMenamin, Phys. Rev. B 6, 3056 (1972).
5. L. Ley, R.A. Pollak, F.R. McFeely, S.P. Kowalczyk, and D.A. Shirley, Phys. Rev. B 9, 600 (1974).
6. C.J. Vesely, R.L. Hengehold, and D.W. Langer, Phys. Rev. B 5, 2296 (1972).
7. D.W. Langer and C.J. Vesely, Phys. Rev. B 2, 4885 (1970).
8. L. Fiermans, E. Arijs, J. Vennik and W. Maenhout-van der Vorst, Surf. Sci. 39, 357 (1973).
9. R.A. Pollak, L. Ley, F.R. McFeely, S.P. Kowalczyk, and D.A. Shirley, J. Electr. Spectrosc. 3, 381 (1974).
10. D.E. Eastman and W.D. Gubman, Phys. Rev. Lett. 28, 1327 (1972).
11. W.C. Price, A.W. Potts, and D.G. Streets, in Electron Spectroscopy, ed. by D.A. Shirley (North-Holland, Amsterdam, 1972).
12. I. Lindau and W.E. Spicer, J. Electr. Spectrosc. 3, 409 (1974).

Appendix A

We are concerned with solving Eq. 5.5:

$$N_{\text{tot}} = I_0 n \sigma \int_0^\infty e^{-\sigma n z} dz \int_{\text{upper hemisphere}} e^{-z/\tau \cos \theta} d\Omega / 4\pi.$$

Integrating with respect to  $\theta$  and using the substitution  $-d \cos \theta = \sin \theta d\theta$  we obtain:

$$N_{\text{tot}} = \frac{I_0 \sigma n (-1)}{2} \int_0^{\pi/2} d(\cos \theta) \int_0^\infty dz e^{-z(\sigma n + \frac{1}{\tau \cos \theta})}. \quad (\text{A.1})$$

The  $dz$  integral is equivalent to  $\int_0^\infty du e^{-u}$  so that

$$N_{\text{tot}} = \frac{-I_0 \sigma n \tau}{2} \int_0^{\pi/2} d(\cos \theta) \frac{\cos \theta}{1 + a \cos \theta} \quad (\text{A.2})$$

where  $a = \sigma n \tau$ . Now let  $u = \cos \theta$  and then

$$N_{\text{tot}} = \frac{-I_0 \sigma n \tau}{2} \int_1^0 du \frac{u}{1+au}. \quad \text{This reduces to}$$

$$N_{\text{tot}} = \frac{+I_0 \sigma n \tau}{2} \left\{ \frac{u}{a} - \frac{1}{a^2} \ln|1 + au| \right\} \Big|_1^0 \quad (\text{A.3})$$

which is equal to  $N_{\text{tot}} = \frac{+I_0 \sigma n \tau}{2} \left\{ \frac{1}{a} - \frac{1}{a^2} \ln|1 + a| \right\}$ .

Dividing both sides of this equation by  $I_0$  to obtain the same quantity as the experimentalists results in:

$$\frac{N_{\text{tot}}}{I_0} = \frac{1}{2} \left\{ 1 - \frac{\ln(1 + \sigma n \tau)}{\sigma n \tau} \right\}. \quad (\text{A.4})$$

APPENDIX B

Using the solid model discussed in Section 5.6.1. we have calculated absolute cross section intensities for the Xray range. However, no absolute intensities for the Xray range have been published in the literature.

Generating the spectra by assuming Gaussian line shapes discussed in Section 5.3. resulted in a normalized curve like that in Figure 5.6 with an O(2s) peak intensity of  $1.1 \times 10^{-6}$ , Zn(3d) peak intensity of  $3.6 \times 10^{-5}$ , and O(2p) peak intensity of  $4.1 \times 10^{-6}$ , all in units of number of electrons emitted per absorbed photon. The scattering depth  $\tau$  assumed was  $20\text{\AA}$ .

C-2

ACKNOWLEDGEMENTS

The author would like to thank Professor Keith H. Johnson for his suggestion of the topic and enlightening discussions and Professor Harry C. Gatos for his support. Many thanks are extended to Harold Kolari, Carl Russo, and especially Christophe Berg for their helpful suggestions. The author would like to express appreciation for continuing help from Martin Frey and the Laboratory for Nuclear Science Computing Facility. And finally, the author's complements go to Maureen Frangioso for her excellent typing.